


**Local structure, bonding, and asymmetry of  $((\text{NH}_2)_2\text{CH})\text{PbBr}_3$ ,  $\text{CsPbBr}_3$ , and  $(\text{CH}_3\text{NH}_3)\text{PbBr}_3$** F. Bridges<sup>1,\*</sup>, J. Gruzdas<sup>1</sup>, C. MacKeen<sup>1</sup>, K. Mayford<sup>1</sup>, N. J. Weadock<sup>2,3</sup>, V. Urena Baltazar<sup>1</sup>, Y. Rakita<sup>4</sup>, Louis Waquier<sup>5</sup>, Julian A. Vigil<sup>6,7</sup>, Hemamala I. Karunadasa<sup>7,8</sup> and M. F. Toney<sup>3,2,9</sup><sup>1</sup>Physics Department, University of California, Santa Cruz, California 95064, USA<sup>2</sup>Department of Chemical and Biological Engineering, University of Colorado at Boulder, Boulder, Colorado 80309, USA<sup>3</sup>Materials Science and Engineering, University of Colorado at Boulder, Boulder, Colorado 80309, USA<sup>4</sup>Department of Materials Engineering, Ben-Gurion University of the Negev, Beer-Sheva 84105, Israel<sup>5</sup>SSRL Materials Science Division, SLAC National Accelerator Laboratory, Menlo Park, California 94025, USA<sup>6</sup>Department of Chemical Engineering, Stanford University, Stanford, California 94305, USA<sup>7</sup>Department of Chemistry, Stanford University, Stanford, California 94305, USA<sup>8</sup>Stanford Institute for Materials and Energy Sciences, SLAC National Accelerator Laboratory, Menlo Park, California 94025, USA<sup>9</sup>Renewable and Sustainable Energy Institute (RASEI), University of Colorado at Boulder, Boulder, Colorado 80309, USA (Received 24 July 2023; revised 16 October 2023; accepted 9 November 2023; published 11 December 2023)

We report local structure measurements for  $\text{CsPbBr}_3$  and  $((\text{NH}_2)_2\text{CH})\text{PbBr}_3$  (FAPbBr<sub>3</sub>) and compare them with recent results for  $(\text{CH}_3\text{NH}_3)\text{PbBr}_3$  (MAPbBr<sub>3</sub>). The Pb-Br bonding is similar for all three systems; the effective spring constants,  $\kappa$ , are comparable (ranging from 1.20 to 1.95 eV/Å<sup>2</sup>), but small in magnitude indicating very soft materials. However, there are also important differences between the three systems. Static disorder is very small for  $\text{CsPbBr}_3$  but increases somewhat with the size of the organic molecular ions MA<sup>+</sup> and FA<sup>+</sup>. At room temperature, dynamic disorder dominates in all compounds. The thermal disorder of the Pb-Br pair distribution function (PDF), i.e., the Debye-Waller factor  $\sigma^2$  follows a correlated Debye or Einstein model up to 300 K in  $\text{CsPbBr}_3$  (orthorhombic phase), but for FAPbBr<sub>3</sub> and MAPbBr<sub>3</sub>, there is a break in the  $\sigma^2(T)$  curve at the orthorhombic-tetragonal transition (o-t) near 150 K, indicating a small change in the spring constant  $\kappa$ .  $\kappa$  increases for MAPbBr<sub>3</sub> but decreases in FAPbBr<sub>3</sub> at this transition. These changes are attributed to changes in the H-bonding between Br<sup>-</sup> and MA<sup>+</sup> or FA<sup>+</sup> at this transition, as a result of librations or rotations of these molecular cations. In addition, the Pb-Br PDF becomes asymmetric at a relatively low temperature for FAPbBr<sub>3</sub> and MAPbBr<sub>3</sub>, while this effect is significantly smaller for  $\text{CsPbBr}_3$ . Finally, we address the question of a model to explain the asymmetric PDF. Two main models are discussed in the literature, an anharmonic pair potential and a split-pair distribution, possibly driven by the presence of a lone pair on the Pb ion. We show that the fourth cumulant  $C_4$  can differentiate between these two models and other possible models. Experimentally  $C_4$  is positive at 250 K and above, for all three systems and that is inconsistent with a split-peak model, for which  $C_4$  is negative for splittings larger than 0.12 Å.

DOI: [10.1103/PhysRevB.108.214102](https://doi.org/10.1103/PhysRevB.108.214102)**I. INTRODUCTION**

The lead halide perovskites continue to be of high importance because of their remarkable properties, particularly those that lead to important applications such as high efficiency solar cells [1,2]. These materials have the usual perovskite stoichiometry,  $\text{APbX}_3$ , where  $A$  is Cs<sup>+</sup>, or an organic cation such as  $\text{CH}_3\text{NH}_3^+$  (MA<sup>+</sup>) or  $(\text{NH}_2)_2\text{CH}^+$  (FA<sup>+</sup>), and  $X$  is a halide, where here we consider Br<sup>-</sup>. In each case, the average crystal structure is orthorhombic (space group  $Pnma$ ) at low temperatures; for the organic cations, the structure is tetragonal at intermediate temperatures (space groups  $P4/mbm$  for FAPbBr<sub>3</sub>,  $I4/mbm$  for MAPbBr<sub>3</sub>), and cubic (space group  $Pm\bar{3}m$ ) at high temperature [3–11]. The  $\text{CsPbBr}_3$  structure remains orthorhombic up to 361 K; where it transforms into a tetragonal phase (space group  $P4/mcm$ )

and then becomes cubic at 403 K. The A-site cations occupy a cuboctahedron space in the  $\text{PbX}_3$  structure and are weakly bonded to the halide anion; for the molecular cations (MA<sup>+</sup> and to a lesser extent, FA<sup>+</sup>), the cation is stationary at low  $T$  but begins to librate or rotate as  $T$  increases through and above the orthorhombic-tetragonal (o-t) transition. [8,12] The transition temperatures for the bromides are given in Table I.

Several investigations of the local structure in these materials all indicate that there is significant asymmetry in the pair distribution function (PDF) for the Pb-Br bond length at 300 K and above. Using EXAFS (extended x-ray absorption fine structure), Singh *et al.* [13] investigated the Pb-Br bond in  $\text{CsPbBr}_3$  and FAPbBr<sub>3</sub> at 300 K and attributed the asymmetry to anharmonicity; similarly, Schuck *et al.* [14] investigated the dynamics of the Pb-I bond in MAPbI<sub>3</sub>, MAPbCl<sub>3</sub> and Cl substituted MAPbI<sub>3</sub>, and also attributed the asymmetry to anharmonicity. On the other hand, Laurita *et al.* [15] used x-ray total scattering (PDF analysis) to investigate a number of halide perovskites above 300 K and modeled the asymmetry

\*Corresponding author: bridges@ucsc.edu

TABLE I. Transition temperatures [3–10] for the orthorhombic to tetragonal (o-t) and tetragonal to cubic (t-c) phase transitions.

Compound	o-t (K)	t-c (K)
MAPbBr <sub>3</sub>	150	235
FAPbBr <sub>3</sub>	153	266
CsPbBr <sub>3</sub>	361	403

assuming that the Pb<sup>2+</sup> ion is off-centered along one of the  $\langle 111 \rangle$  directions, resulting in three longer and three shorter Pb-Br bonds. They used a sum of two Gaussians to describe the PDF of this split peak distribution. We will compare with these works.

Recently we published a combined study of MAPbBr<sub>3</sub> using EXAFS, x-ray diffraction (XRD), and *ab initio* molecular dynamics (AIMD) that showed asymmetry in the Pb-Br pair distribution [16]. Correlations in the motions [17] of the Pb<sup>2+</sup> and Br<sup>-</sup> ions were obtained using a combination of the XRD atomic anisotropic displacement parameters (ADP) and the EXAFS Debye Waller parameter  $\sigma^2$  ( $\sigma$  is the width of the PDF). We showed using a cumulant analysis (see Sec. IV B), that the third cumulant,  $C_3$  (describing the PDF asymmetry), increased quadratically with  $T$ . In addition, the second cumulant  $\sigma^2$  had an unusual  $T$  dependence—it did not follow a Debye or Einstein model for thermal disorder over the entire temperature range from 0 to 300 K. Instead there is a break in the  $\sigma^2(T)$  curve at the orthorhombic-tetragonal phase transition, indicating a change in the effective spring constant for this bond. Those studies raise additional questions which we address here.

**Bonding.** The first relates to bonding and the unexpected change in the Pb-Br effective spring constant,  $\kappa$ , at the orthorhombic-tetragonal (o-t) transition; for MAPbBr<sub>3</sub> [16] this parameter increases by roughly 26%. This change in  $\kappa$  for MAPbBr<sub>3</sub> is obtained from the temperature dependence of  $\sigma^2(T)$  above and below the o-t transition temperature. We will show that a similar change exists for the Pb-Br pair in FAPbBr<sub>3</sub> at this transition. Note that  $\sigma_{\text{Pb-Br}}^2(T)$  in CsPbBr<sub>3</sub> has the expected behavior (i.e., follows an Einstein or correlated Debye model), [18–20] in part because CsPbBr<sub>3</sub> remains orthorhombic up to 300 K. It is as yet unknown if a similar break in the  $\sigma_{\text{Pb-Br}}^2(T)$  curve exists at the o-t transition (361 K) for this material.

**Static disorder.** The fits of  $\sigma^2(T)$  to a correlated Debye model also provide an estimate of any static disorder in the Pb-Br lattice. However all these values of  $\sigma_{\text{static}}^2$  are considered to be quite small - much less than the thermally induced disorder at 300 K, in agreement with Zeiske *et al.* [21]. In MAPbBr<sub>3</sub>, different values of  $\sigma_{\text{static}}^2$  are needed above and below the o-t transition. At high  $T$ ,  $\sigma_{\text{static}}^2 \approx 0.0022 \text{ \AA}^2$ , and comparable to the zero-point-motion contribution at low  $T$ , while in the orthorhombic phase,  $\sigma_{\text{static}}^2$  is 7 times smaller. We also show that  $\sigma_{\text{static}}^2$  in CsPbBr<sub>3</sub> is very small, roughly  $0.0002 \text{ \AA}^2$ , while in FAPbBr<sub>3</sub> this parameter again changes at the o-t transition; it is quite small in the high  $T$  regime ( $0.0007 \text{ \AA}^2$ ), but larger in the orthorhombic regime ( $0.0045 \text{ \AA}^2$ ). Reuveni *et al.* [22] report significant static disorder in FAPbBr<sub>3</sub> using a combination of XRD and Raman experiments; however their

arguments are qualitative (no numbers provided). From our measurements, however,  $\sigma_{\text{static}}^2$  is fairly small in this system, and there may be some disagreement.

**Asymmetry and anharmonicity.** A third issue is the deviation of the PDF from a Gaussian function which is now recognized by many researchers for the perovskites [14,15,23] and used much earlier for other materials [24]. Small deviations from a Gaussian are often parameterized in terms of higher order cumulants ( $C_n$ ;  $n \geq 3$ );  $C_3$  models the skewness, and  $C_4$  models a symmetric distortion related to kurtosis (see Sec. IV B). However there are disagreements as to the actual shape of the PDF at higher temperatures, and usually only one model is discussed by most authors. Some researchers (Liu *et al.* [23], Schuck *et al.* [14]) attribute such deviations to an anharmonic potential such as a Morse potential and use the data to determine the potential parameters. Others, such as Laurita *et al.* [15] report a split peak as a result of Pb shifting off-center, and model the PDF as a sum of two Gaussians; for MAPbBr<sub>3</sub> and FAPbBr<sub>3</sub> the splitting is  $\approx 0.14 \text{ \AA}$  [15]. This model is based on the assumption that the Pb lone pair shifts the Pb atom off-center along the  $\langle 111 \rangle$  directions in the crystal. The resulting PDFs for different approaches can be very similar. We show four examples of asymmetric distributions and discuss how anharmonic potentials and split-peak models can be differentiated using the fourth cumulant.

**Isosbestic points and an experimental relationship between  $\sigma^2$  and  $C_3$ .** While investigating structure in the  $k$ -space data related to asymmetry, isosbestic points were found at which all curves cross at the same value of  $k = k_{ib,n}$ , independent of temperature. This means that at these values of  $k$ , there is a relationship between the amplitude of the EXAFS function  $\chi(k)$  and its phase. We will show that this leads to an experimental relationship between the second and third cumulants ( $\sigma^2$  and  $C_3$ ).

**Cs<sup>+</sup>-Br<sup>-</sup> bonds.** Finally we also consider the strength of the bonding between the A-site cation Cs<sup>+</sup> and Br<sup>-</sup> in CsPbBr<sub>3</sub>; EXAFS can directly probe this bonding using Cs  $K$  edge EXAFS. We will show that the effective spring constant for the shortest Cs-Br pair is significantly weaker than for Pb-Br. Using EXAFS to investigate similar bonding between Br<sup>-</sup> and the organic ions is not feasible.

## II. SAMPLE PREPARATION AND DATA COLLECTION

High-quality crystals of FAPbBr<sub>3</sub> were grown following Ceratti *et al.* [25]; similar procedures for CsPbBr<sub>3</sub> are given in Rakita *et al.* [26]. For each material several crystallites were ground to a fine powder following the procedures outlined for MAPbBr<sub>3</sub> [16]. The resulting powders were spread on tape using a fine brush which removed larger particles. Two layers of tape were pressed together to form a double layer and three double layers were stacked for the Pb  $L_{III}$  and Br  $K$  edges, with the samples at  $90^\circ$  to the beam. For the high energy Cs  $K$  edge, twelve double layers were stacked, and the sample probe was rotated to  $30^\circ$  to the beam to double the path length. Also for the Cs  $K$  edge (36 keV), Ar gas was used for the ionization chambers.

Data were collected on beamline 4-1 at the Stanford Synchrotron Radiation Lightsource (SSRL) using a double monochromator with Si (220) crystals. The temperature was

controlled using an Oxford helium cryostat over the range 5–300 K. For the Pb  $L_{III}$  and Br  $K$  edges the vertical slit size was 0.4 mm, while for the high energy Cs  $K$  edge it was reduced to 0.2 mm, so that in each case the monochromator energy resolution was below the core-hole lifetime broadening energy. To reduce harmonics, the monochromator was detuned 30% at the Pb and Br edges and 20% at the Cs  $K$  edge. Because the Pb  $L_{III}$  and Br  $K$  edges are close together there is a small remnant of the Pb EXAFS that had to be subtracted from the Br  $K$  edge data, as outlined in a previously published Supplemental Information (SI). [16]

The absorption data were reduced using the programs in RSXAP [27]; “reduce” incorporates standard techniques to remove the backgrounds, both below and above the edge. After removing the pre-edge background, the edges were normalized just above the edge. The presence of the Br  $K$  edge, just 439 eV above the Pb  $L_{III}$  edge [16], limits the  $k$  range to about  $10.2 \text{ \AA}^{-1}$ .

Examples of the  $k$ -space data for the Pb  $L_{III}$  edge in FAPbBr<sub>3</sub>, and all three edges in CsPbBr<sub>3</sub>, (Pb  $L_{III}$ , Br  $K$ , and Cs  $K$  edge) are given in Ref. [28], Figs. S1 and S2; see also Refs. [29–31]. Unfortunately, the data for the Br  $K$  edge in FAPbBr<sub>3</sub> were noisy (had steps) and were not used.

#### A. CsPbBr<sub>3</sub> single crystal preparation and diffraction data collection

Crystals suitable for single crystal x-ray diffraction (SXR) measurements were obtained by vapor diffusion. Solid CsBr (0.383 g, 1.80 mmol) and PbBr<sub>2</sub> (0.661 g, 1.80 mmol) were combined in dimethyl sulfoxide (4 mL) and stirred for 12 h at 50 °C; a saturated solution was produced following a reported procedure [26] wherein acetonitrile was added dropwise up to a ratio of 1.1:1 (vol. acetonitrile: vol. dimethyl sulfoxide). The resulting solution was then stirred for 24 h before any remaining solid was removed by filtration through a 0.22- $\mu\text{m}$  filter. Then, 1 mL of this precursor solution was transferred to a small shell vial and placed within a 20 mL scintillation vial that was previously charged with antisolvent (3 mL). We found that smaller crystals suitable for measurement were obtained with a mixed antisolvent of acetonitrile and diethyl ether (1:2-2:1 vol. acetonitrile : vol. diethyl ether); crystallizations using neat acetonitrile [26] as the antisolvent produced larger crystals. The vials were sealed and stored in the dark for multiple days before isolating the resulting crystals. All crystallizations were left undisturbed for at least 16h, and some crystals were stored for more than a week in the mother liquor after the vapor diffusion reached equilibrium before isolating for measurement.

Suitable CsPbBr<sub>3</sub> single crystals were mounted on an x-ray transparent MiTeGen microloop using Paratone oil. Single crystal x-ray diffraction (SXR) data were collected on a Bruker D8 Venture diffractometer equipped with a Photon 100 CMOS detector. The sample temperature was varied from 100–300 K with an Oxford Cryostream. Data were collected with  $\phi$  and  $\omega$  scans using Mo- $K_{\alpha}$  radiation ( $\lambda = 0.71073 \text{ \AA}$ ). Frames were integrated using SAINT V8.38A and absorption correction was performed with SADABS-2016/2, both in the BRUKER APEX 3 software. The initial space group assignment was made with XPREP based on reported structures,

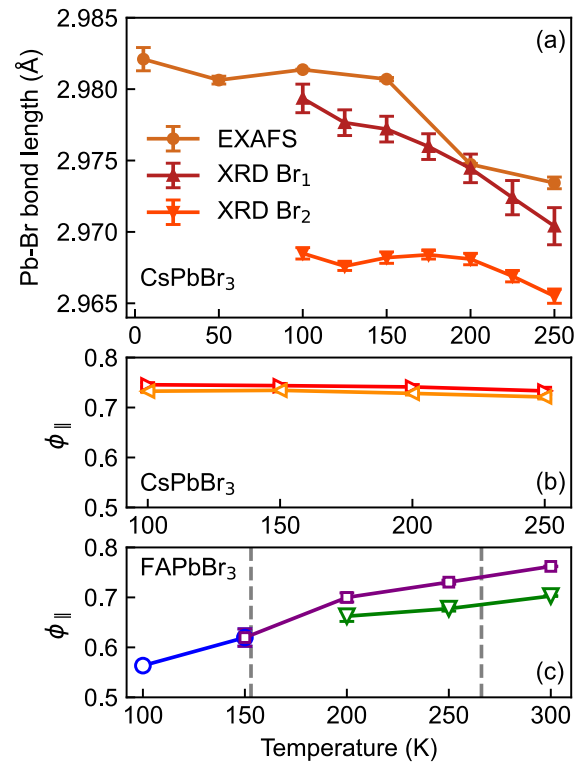


FIG. 1. (a) Nearest-neighbor Pb-Br bond lengths in CsPbBr<sub>3</sub> obtained from EXAFS (circles) and SXR (triangles). Note that there are two crystallographically distinct Br sites observed in XRD, both are reported here. (b) Pb-Br  $\phi_{\parallel}$  for crystallographically distinct Br atoms in CsPbBr<sub>3</sub>. The correlation coefficients are only calculated for temperatures measured with both SXR and EXAFS. (c) Pb-Br  $\phi_{\parallel}$  calculated for FAPbBr<sub>3</sub> using published SXR data and EXAFS data from this work. Blue circles represent  $\phi_{\parallel}$  calculated from  $\sigma^2$  values extrapolated from the low temperature correlated Debye model fits, green upside-down triangles are  $\phi_{\parallel}$  calculated from high temperature correlated Debye model fits, and purple squares are  $\phi_{\parallel}$  calculated from low temperature correlated Debye model fits extrapolated to high temperatures. The gray vertical lines in (c) mark the structural phase transition temperatures. Error bars may be smaller than the corresponding symbol.

systematic absences,  $|E * E - 1|$  statistics, and refinement statistics. The structure was solved using direct methods with the SHELXT software [32] and refined using a least-squares method implemented by SHELXL-2014/7 in the OLEX 2 software package. The thermal displacement parameters for Cs, Pb, and Br are all refined anisotropically.

### III. XRD DATA

The crystal structure of CsPbBr<sub>3</sub> was solved at several temperatures from 100–300 K with single crystal x-ray diffraction (SXR) as described above. Tables of the results are provided in Ref. [28] in Sec. VIII. At all temperatures, the crystal structure is  $Pnma$ . We use these obtained structures as input for the initial EXAFS fits described below. The average nearest neighbor Pb-Br bond length  $R_C$  is compared with the EXAFS Pb-Br bond length  $r_{\text{avg}}$  in Fig. 1(a). Both  $R_C$  and  $r_{\text{avg}}$  decrease with increasing temperature, and  $r_{\text{avg}}$  is greater than

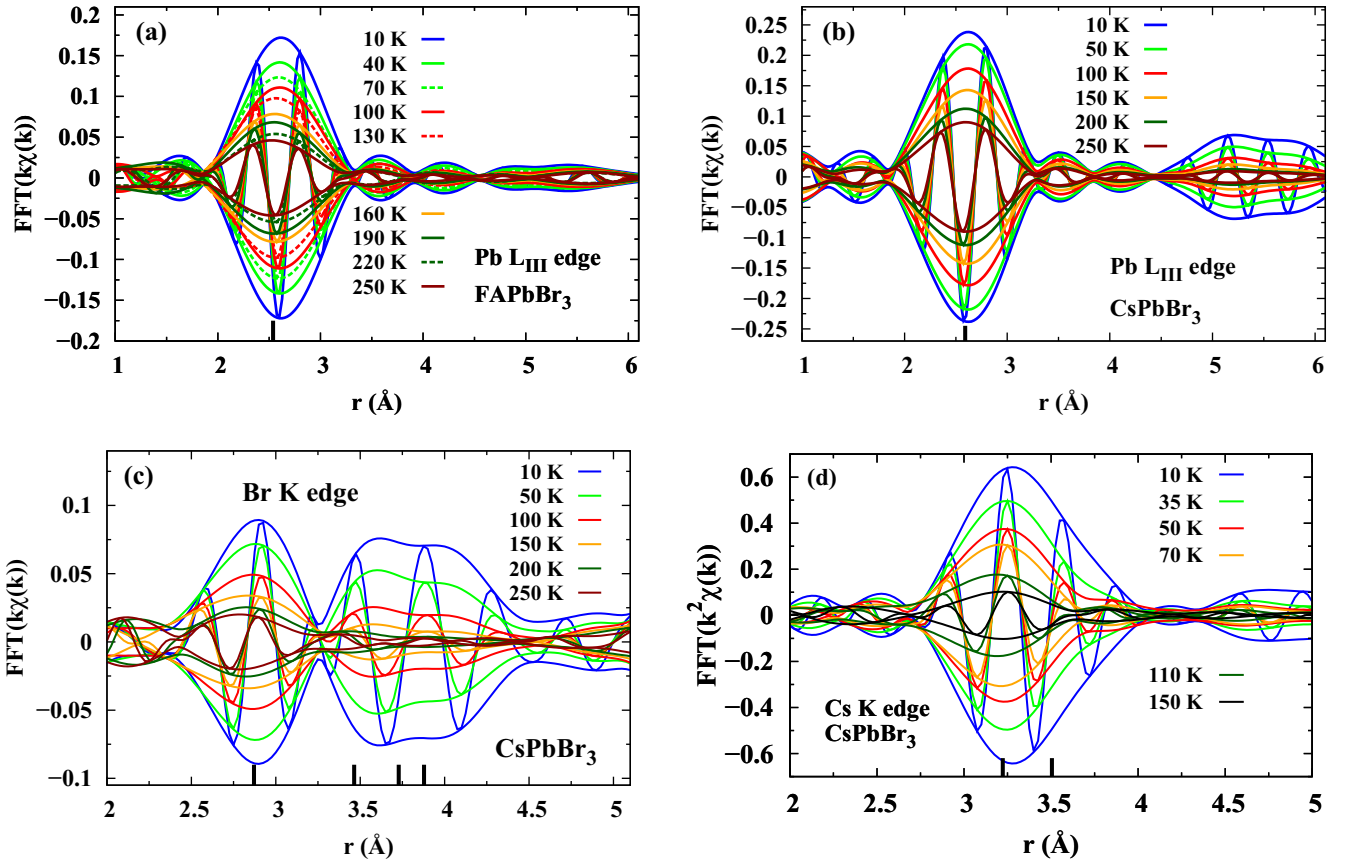


FIG. 2.  $r$ -space data for the Pb  $L_{III}$  in (a) FAPbBr<sub>3</sub>, (b) CsPbBr<sub>3</sub>, the Br  $K$  edge in (c) CsPbBr<sub>3</sub>, and the Cs  $K$  edge in (d) CsPbBr<sub>3</sub>, as a function of temperature. The fast oscillating function is the real part of the FT,  $R$ , while the amplitude function is given by  $\sqrt{R^2 + I^2}$  where  $I$  is the imaginary part of the transform. For Pb  $L_{III}$  edge data (a) and (b), the first peak is for the Pb-Br pair and the expected position on the EXAFS plot (based on diffraction results) is near 2.6 Å. For the Br  $K$  edge (c) the first four peaks are: Br-Pb, Br-Cs, a second Br-Cs, and Br-Br. For the Cs  $K$  edge (d), the signal to noise is high at low  $T$  and we have used a  $k^2$  weighting. The first shell is a sum of two overlapping Cs-Br peaks, and each trace is the average of 4–5 scans. The FT range for the Pb data is 3.5–9.8 Å<sup>-1</sup>, that for Br data is 5–13 Å<sup>-1</sup>, while the FT range for the Cs  $K$  edge is 3.5–12.6 Å<sup>-1</sup>, all Gaussian broadened by 0.2 Å<sup>-1</sup>. In each case, the expected positions on the EXAFS plot, based on pair distances from diffraction, are shown as black bars along the x-axis.

$R_C$ . The latter behavior is expected due to the fact that  $r_{\text{avg}}$  incorporates instantaneous thermal displacements (including transverse motion), whereas  $R_C$  is the distance between average atomic positions. Note that although  $r_{\text{avg}}$  usually increases with  $T$ , if the decrease of  $R_C$  with  $T$  is sufficient, it will also make  $r_{\text{avg}}$  decrease.

The anisotropic thermal displacement parameters (ADPs) are compared with EXAFS  $\sigma^2$ , *vide infra*, to calculate the correlation coefficient  $\phi_{\parallel}$  of Pb-Br motions as described in Sec. IV of Ref. [28]. The results, plotted in Fig. 1(b), show that the Pb-Br motion is strongly correlated and  $\phi_{\parallel}$  only decreases slightly with increasing temperature.

Fig. 1(c) plots the Pb-Br  $\phi_{\parallel}$  for FAPbBr<sub>3</sub> calculated from the EXAFS  $\sigma^2$ , *vide infra*, and FAPbBr<sub>3</sub>  $R_C$  and ADPs reported in the literature [22]. We note that the reported structures were refined in the simple cubic  $Pm\bar{3}m$  phase at all temperatures. The  $\sigma^2$  values used to calculate  $\phi_{\parallel}$  were obtained from the correlated Debye model fits described in Sec. IV D. The Pb-Br  $\phi_{\parallel}$ , is moderate at low temperatures and continually increases with temperature with a slight jump at the orthorhombic-tetragonal transition. An increase in  $\phi_{\parallel}$  with temperature is unusual but has been reported for MAPbBr<sub>3</sub>

[16]. For MAPbBr<sub>3</sub>, however, the increase in  $\phi_{\parallel}$  occurs only at the orthorhombic-tetragonal transition before decreasing with increasing temperature.

Results of the SXRD structure solutions are reported in Ref. [28], Tables I–X. Our results strongly agree with those of López *et al.* [33]. The lower symmetry structures proposed by S. Liu, *et al.* [34], who use high-quality synchrotron XRD to resolve weak peaks, were not considered here. However, the reported crystallographic density values and anisotropic displacement parameters are in good agreement with our results.

## IV. EXAFS DATA AND ANALYSIS

### A. EXAFS $r$ -space data

The  $k$ -space data, plotted in Figs. S1 and S2 in Ref. [28], were Fourier transformed (FT) into  $r$ -space using the FT ranges 3.5–9.8 Å<sup>-1</sup> for the Pb  $L_{III}$  and 5–13 Å<sup>-1</sup> for the Br  $K$  edge. The  $r$ -space plots are shown in Fig. 2; each trace is the average of 3 scans. On EXAFS  $r$ -space plots, the peak positions are shifted to a shorter  $r$  relative to the pair distance determined from XRD, as a result of the  $\phi(k)$  function [35] [see Eq. (1)]; and these shifted positions are



noted by black bars, along the  $x$  axis. The strong temperature dependence of the  $r$ -space plots is shown in Fig. 2 for the Pb, Br, and Cs edges. Also note the amplitude difference at the Pb edge between FAPbBr<sub>3</sub> and CsPbBr<sub>3</sub> [Figs. 2(a) and 2(b)]. The significantly lower amplitude for FAPbBr<sub>3</sub> at comparable temperatures means the environment about Pb in this material is more disordered than in CsPbBr<sub>3</sub>. This will show up in the  $\sigma^2(T)$  results discussed later (Sec. IV D) and is a combination of static and thermal disorder. This increased disorder for FAPbBr<sub>3</sub> also contributed to the smaller signal observed at the Br  $K$  edge.

The Cs  $K$  edge  $r$ -space data for CsPbBr<sub>3</sub> are plotted in Fig. 2(d) up to 150 K—for higher  $T$  the  $k$ -space data amplitude is approaching the noise level for much of the  $k$  range. On the  $r$ -space plot, the amplitude at 150 K has dropped by a factor of 6 compared to the 10 K data. The first shell about Cs has two overlapping Cs-Br peaks (actual distances at 100 K are  $\approx 3.64$  and  $3.92$  Å), while the second shell above  $4.4$  Å, is mostly Cs-Pb pairs but has some contribution from longer Cs-Br pairs. We will focus on the first shell only and primarily on the peak near  $3.2$  Å [Fig. 2(d)], in the later fits of the Cs  $K$  edge data.

### B. EXAFS equation

The standard EXAFS equation for a pair of atoms assumes a Gaussian function, which is an excellent approximation for low  $T$ . The parameters used to describe this PDF are the number of neighbors, the average pair-distance (first moment/cumulant) and  $\sigma^2$  (second moment/cumulant), where  $\sigma$  is the width of the PDF. For the Gaussian distribution, all higher order cumulants are zero. When the distribution deviates from a Gaussian—symmetric or slightly sharpened/flattened—and this deviation is small, the EXAFS equation for an atom-pair can be extended by including higher order cumulants (Note: using cumulants is more useful than using the moments of the distribution [36–38]). Including the third and fourth cumulants (related to the third and fourth moments of the distribution) the function  $k\chi_{Pb-Br}(k)$  for the first Pb-Br peak in the Pb  $L_{III}$  data has the form

$$k\chi_s(k, r) = A_o \sin \left( 2kr - \frac{4}{3}C_3k^3 + \phi(k) \right),$$

$$A_o = \frac{NS_0^2}{r^2} F(\pi, k) e^{-2r/\lambda(k) + \frac{2}{3}C_4k^4},$$

$$k\chi_{Pb-Br}(k) = \int_0^\infty g(r, \sigma, R_o) k\chi_s(k, r) dr. \quad (1)$$

Here  $g(r, \sigma, R_o)$  is a Gaussian function, centered at  $R_o$ , with width  $\sigma$ , while the cumulants  $C_3$  (a measure of skewness of the PDF) and  $C_4$  (a measure of the kurtosis—a flattening/sharpening of the PDF) are small corrections. In Eq. (1), the integral is over  $g(r, \sigma, R_o)/r^2$ , not just  $g(r, \sigma, R_o)$  and is evaluated numerically each time some parameter is varied [39]; consequently, additional corrections to the phase of the sine function that are present in some formulations are not needed (see Ref. [28]). If the deviations from a Gaussian are too large (i.e., some  $C_n$  are too large), the cumulant expansion does not converge [36,38]; this occurs when  $k_{\max} * C_n^{1/n}$

approaches 1.0 ( $k_{\max}$  is the highest useful value on a  $k$ -space plot). For our Pb edge data,  $k_{\max}$  is  $10 \text{ \AA}^{-1}$  (limited by the Br  $K$  edge) and this limit is reached when  $C_3 \approx 0.001 \text{ \AA}^3$ ; our highest  $T$  data point for  $C_3$  is close to this limit. For larger distortions of the distribution function an asymmetric PDF must be used for  $g(r, \sigma, R_o)$  (and the parameters  $C_3$  and  $C_4$  are removed), as done by Yang *et al.* using the  $\Gamma$ -function distribution [38]. The values of  $C_3$  and  $C_4$  can still be determined from calculations of the moments for a specific distribution.

For the first Pb-Br peak in the  $r$ -space data [using Eq. (1)],  $N$  is the number of Br neighbors,  $S_0^2$  is the amplitude reduction factor which accounts for multielectron effects,  $F(\pi, k)$  is the backscattering amplitude of the photoelectron wave,  $\phi(k)$  is the phase factor arising from the excited and back-scattering atoms ( $F$  and  $\phi(k)$  are calculated using FEFF7 [40]),  $\lambda$  is the mean free path (the term  $e^{-2r/\lambda(k)}$  is often combined together with  $F$ ), and  $\sigma^2$  is the variance of the pair distribution function, usually called the Debye-Waller factor.  $\sigma^2$  primarily affects the amplitude in  $r$ -space and the resulting amplitude damping as a function of  $k$  is modeled by  $\exp(-2k^2\sigma^2)$ . Note that  $C_3$  only affects the phase while  $\sigma^2$  affects the amplitude and thus these two parameters are nearly independent—very little correlation. In contrast  $C_4$  and  $\sigma^2$  are highly correlated.  $C_4$  is most important at high  $k$  [i.e., the exponent is  $(2/3)C_4k^4$ ], and because of the limited  $k$ -range for the Pb  $L_{III}$  edge data, fits are less sensitive to  $C_4$  until  $T$  is close to 300 K. Finally, the leading term in the atomic phase,  $\phi(k)$ , is linear in  $k$  [i.e.,  $\phi(k) = -\Delta * (2k)$  plus a slowly varying term,  $f(k)$ ] and leads to a negative shift of the peak position (by  $-\Delta$ ) on an EXAFS plot.

### C. Fits in $r$ -space

The  $r$ -space data for each edge consists of a series of peaks, many of which partially overlap. For the Pb  $L_{III}$  edge data, the first peak is well separated from further neighbor peaks and one-peak fits were carried out for all Pb  $L_{III}$  edge data, using a FEFF7 [40] function for Pb-Br, and varying parameters  $r$ ,  $\sigma$ , and  $C_3$  (and also  $C_4$  at the higher temperatures).  $S_0^2$  was set to 0.99 for the Pb  $L_{III}$  edge from previous measurements [16] and  $N = 6$  (six Br neighbors) for this structure. The effects from  $C_3$  will be discussed in more detail in a later section (see Sec. IV E). The  $C_4$  parameter has much larger errors in part because the values of this parameter are sensitive to the  $k$ -range used.

For the Br  $K$  edge in CsPbBr<sub>3</sub>, unlike in FAPbBr<sub>3</sub> or MAPbBr<sub>3</sub>, there are significant further neighbor peaks—see Fig. 2(c). These peaks partially overlap the Br-Pb peak at  $2.7$  Å, and a four-peak fit was carried out. There are two Br-Cs peaks (XRD-based distances near  $3.64$  and  $3.92$  Å in the orthorhombic phase; bars on the  $x$  axis show positions on an EXAFS plot), and because of the distorted structure and the presence of two distinct Br sites (there are twice as many Br<sub>2</sub> sites as Br<sub>1</sub> sites), the average number of neighbors for each of these pairs is  $4/3$ . Other Br-Cs peaks are at significantly longer distances and do not contribute up to  $4.1$  Å. Note that there are eight Br neighbors at a distance near  $4.21$  Å. These Br-Br pair distances are slightly split, about  $\pm 0.05$  Å, which cannot be resolved in EXAFS. Although a four-peak fit is

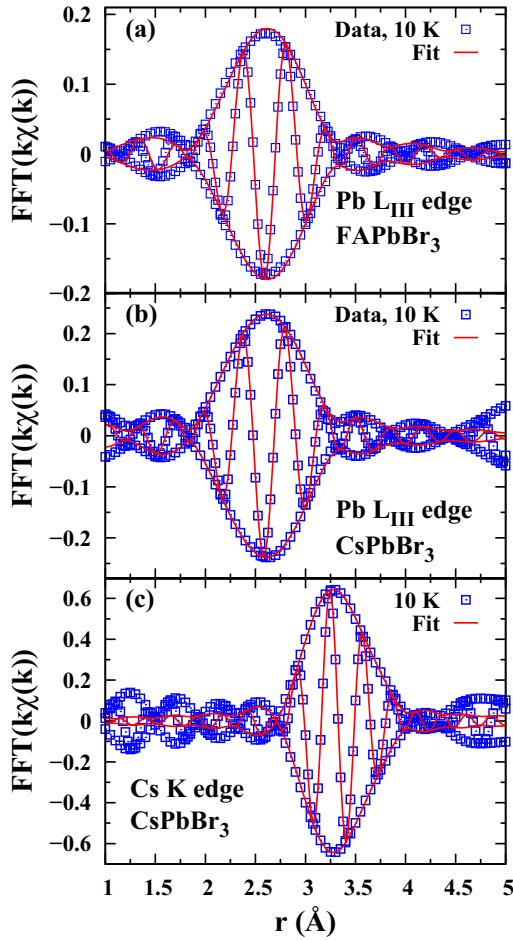


FIG. 3. Examples of fits at 10 K: (a) the Pb  $L_{III}$  edge in FAPbBr<sub>3</sub>, (b) the Pb  $L_{III}$  edge in CsPbBr<sub>3</sub>, and (c) the Cs  $K$  edge in CsPbBr<sub>3</sub>. The Pb  $L_{III}$  edge fits are one-peak fits while the Cs  $K$  edge fit is a two-peak fit (two partially overlapping Cs-Br peaks).

needed for the Br edge, we will focus on the Br-Pb parameters to compare with results for Pb-Br.

For the Cs  $K$  edge in CsPbBr<sub>3</sub> [Fig. 2(d)], the first peak is a sum of two Cs-Br peaks in the orthorhombic phase (XRD-based distances near 3.64 and 3.92 Å). The expected distances on an EXAFS plot, are shown as bars on Fig. 2(d); note that the second peak damps rapidly with  $T$ , and is not visible above 70 K, due to increased thermal disorder. For each peak there are four Br neighbors. Again, for both the Br and Cs  $K$  edges, the parameters  $r$  and  $\sigma$  are varied in the fitting. Examples of the fits at 10 K for the Pb  $L_{III}$  edge in FAPbBr<sub>3</sub> and CsPbBr<sub>3</sub>, and the Cs  $K$  edge in CsPbBr<sub>3</sub> are shown in Fig. 3.

#### D. $\sigma^2(T)$ results

In Fig. 4,  $\sigma^2(T)$  is plotted for the Pb-Br peak in each Pb data set. The  $\sigma^2$  plot for Pb-Br in CsPbBr<sub>3</sub>, shows the usual behavior, a curve that is a straight line at high  $T$  but goes to a nonzero constant as  $T$  goes to 0; this result is independent of using  $k$  or  $k^2$  weighting in the EXAFS analysis. The surprising result on this plot is that for those materials containing the organic ions, MA<sup>+</sup> or FA<sup>+</sup>, (MAPbBr<sub>3</sub> or FAPbBr<sub>3</sub>), there

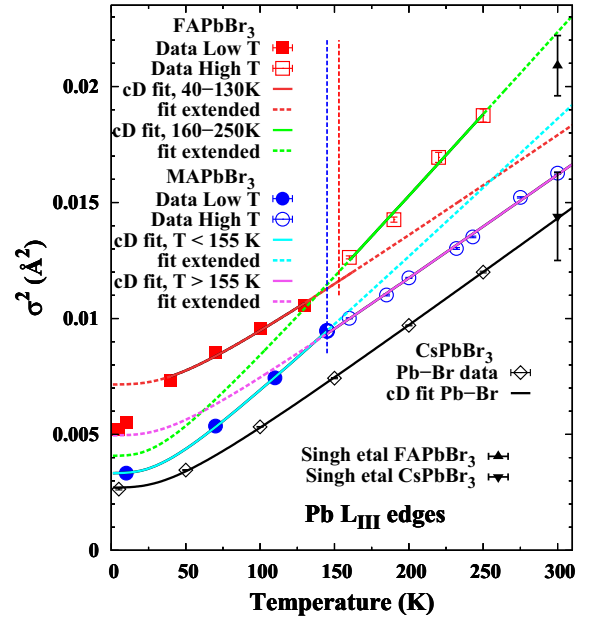


FIG. 4.  $\sigma^2(T)$  plots for the Pb-Br pair in FAPbBr<sub>3</sub> (red), MAPbBr<sub>3</sub> (blue), and CsPbBr<sub>3</sub> (black). The plot for CsPbBr<sub>3</sub> shows a typical temperature dependence and also a low static contribution. The plot for MAPbBr<sub>3</sub> (data from earlier paper [16]), has a clear break in the curve near 145 K and the static contribution at low  $T$  is also small; however when only fitting data above 150K, the static off-set is much higher. The plot for FAPbBr<sub>3</sub> has a similar break in slope near 150 K, but here the slope increases above 150 K. The values for  $\sigma_{\text{static}}^2$  are as follows: CsPbBr<sub>3</sub>, 0.00019(6) Å<sup>2</sup>; MAPbBr<sub>3</sub>, low  $T$  fit, 0.00035(5) Å<sup>2</sup>; FAPbBr<sub>3</sub>, fit 30–130 K, 0.0046(3) Å<sup>2</sup>. In addition, there is also an anomaly at low  $T$ , for  $T \leq 10$  K. For most cases, the relative error bars are smaller than the symbols and comparable to the scatter of the points about each fit line. Data points at 300 K from reference [13], are also included as black triangles for FAPbBr<sub>3</sub> and CsPbBr<sub>3</sub>; note the larger errors at 300 K. The o-t transitions are noted by vertical dashed lines.

is a kink in  $\sigma^2(T)$  near the orthorhombic to tetragonal phase transitions, at  $\approx 145$  and 153 K, respectively.

For MAPbBr<sub>3</sub>, the slope decreases significantly above  $\approx 150$  K, while for FAPbBr<sub>3</sub>, the slope increases above the transition temperature (near 153 K) [10]. This means that the effective spring constant,  $\kappa$ , becomes stiffer for MAPbBr<sub>3</sub> but weaker for FAPbBr<sub>3</sub>—see Fig. 4. For the latter, it is surprising that  $\kappa$  would be higher below 150 K (with a value comparable to the value for MAPbBr<sub>3</sub> at high  $T$ ). One further unexpected feature for FAPbBr<sub>3</sub> is that  $\sigma^2$  at low  $T$  ( $\leq 10$  K) is significantly lower than expected, when compared to the data in the 40–145 K range. This was recognized while collecting data; after the data collection was finished (21 hours later), a second low temperature scan, on the same point on the sample, was collected at 5 K. Within errors this result is identical to that for our first data point at 10 K. This is a check that there is no sample damage from the intense x-ray beam as also reported at 300 K by Singh *et al.* [13] Details for the FAPbBr<sub>3</sub> and CsPbBr<sub>3</sub> samples are given as separate plots in Ref. [28] (Fig. S3) including also the correlated Debye temperatures and static off-sets discussed below.

$\sigma^2$  is a measure of the disorder in a crystal and for most well ordered materials this disorder is primarily thermal in nature, with a small static contribution. Two models are used to calculate the phonon contribution—the Einstein model and the correlated Debye model; the former uses a single phonon frequency while the correlated Debye model is a weighted sum over a range of frequencies—see Eq. (2). The main difference in the two models is a slight change in curvature in the low to moderate temperature range; at high  $T$  they are identical.

The equation [18,19,41] for the correlated-Debye (cD) model is given by

$$\sigma_{cD}^2 = \frac{3\hbar}{2M_R} \int_0^{\omega_D} \frac{\omega}{\omega_D^3} C_{\text{pair}} \coth\left(\frac{\hbar\omega}{2k_B T}\right) d\omega + \sigma_{\text{static}}^2; \quad (2)$$

where  $\omega_D$  is the Debye frequency with corresponding Debye wave number  $k_D$ ,  $M_R$  is the reduced mass,  $C_{\text{pair}}$  is a correlation function given by  $1 - \sin(\omega r_{\text{avg}}/c)/(\omega r_{\text{avg}}/c)$ ,  $r_{\text{avg}}$  is the average pair distance, and  $c = \frac{\omega_D}{k_D}$ . The similar equation for the Einstein model is given in Ref. [28], Eq. (S1). In both cases,  $\sigma_{\text{static}}^2$  is the static offset from nonthermal broadening, and  $\sigma^2(T \sim 0)$  with zero static offset gives the zero-point motion contribution for a given atom-pair. Note that  $\sigma_{\text{static}}^2$  is smaller than the zero-point motion contribution in these materials; it changes slightly when the crystal structure changes from orthorhombic to tetragonal [and the fit of  $\sigma^2(T)$  to the correlated Debye model is extrapolated to  $T = 0.0$ ], but we do not consider that a thermally induced change in  $\sigma^2$ .

Of these perovskites, CsPbBr<sub>3</sub> has the least static disorder for the Pb-Br pair; the fit shown in Fig. 4 gives  $\sigma_{\text{static}}^2 = 0.00019 \text{ \AA}^2$ . The cD fits for the Pb-Br pairs in MAPbBr<sub>3</sub> and FAPbBr<sub>3</sub> have a break in the curve at the o-t transition leading to different values of  $\sigma_{\text{static}}^2$  in the low  $T$  and high  $T$  regimes; see Fig. S3 in Ref. [28]. For FAPbBr<sub>3</sub>, however, at low  $T$ , the lowest temperature points do not fit the cD model and even the point at 40 K is low (particularly if this point is not included in the fits). A possible model is that  $\sigma_{\text{static}}^2$  is not a constant for FAPbBr<sub>3</sub> but instead starts small and increases slightly with  $T$ . Because of the large size of the FA<sup>+</sup> molecular cation and the apparently very strong bonding between Br<sup>-</sup> and some H<sup>+</sup> ions[13], as the FA<sup>+</sup> cation begins to move or librate it locally displaces some Br<sup>-</sup> ions, straining the lattice and leading to increased Pb-Br disorder; eventually motions of the FA ion will locally break the hydrogen bond and that limits the level of distortion. A plot of  $\sigma_{\text{static}}^2(T)$  for such a possible model is provided in Fig. S5 in Ref. [28].

An important feature of both the cD and Einstein models is that at high  $T$ ,  $\sigma^2 = k_B T/\kappa$  where  $k_B$  is Boltzmann's constant and  $\kappa$  is the effective spring constant which includes small contributions from the surrounding lattice.  $\kappa$  is independent of the model used (Einstein or Debye) and is easily extracted from the slope of  $\sigma^2$  versus  $T$  at high temperature, which can be obtained from fits of the  $\sigma^2(T)$  data. Then with  $T$  extended to high temperatures,  $\kappa$  is given by

$$\kappa = \frac{k_B}{d(\sigma^2)/dT}. \quad (3)$$

The main contribution to  $\kappa$  is the direct bonding to neighboring ions via shared charge. Here we use the ‘‘bond-

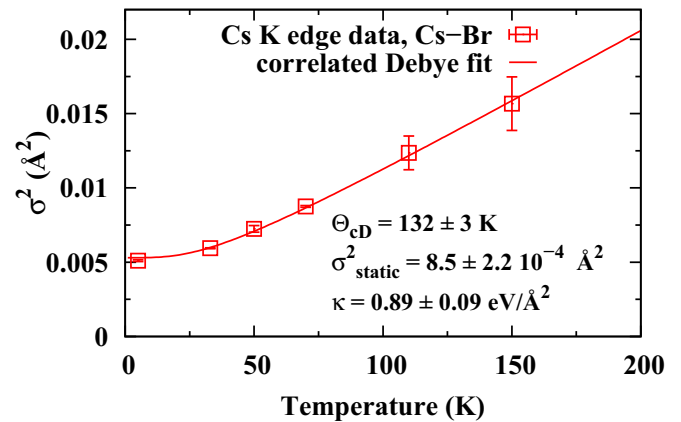


FIG. 5.  $\sigma^2(T)$  for the first Cs-Br pair at the Cs  $K$  edge. For this pair, the effective spring constant is small as expected for the longer Cs-Br bond length; the large error in  $\kappa$  arises from the larger uncertainty for the values of  $\sigma^2$  at 110 and 150 K.

valence’’ model [42–44] as a guide. In this model, the contribution to the valence (and hence charge sharing) for each neighboring ion, is strongly dependent on the individual bond lengths. Pb<sup>2+</sup> is primarily bonded to the 6 neighboring Br<sup>-</sup> ions and the bond strength will depend on the distributions of charge on both ions and the individual Pb-Br bond lengths. In contrast, Br<sup>-</sup> is bonded to two types of positive ions; two Pb<sup>2+</sup> ions and four A-site cations, such as Cs<sup>+</sup>. In the orthorhombic phase (CsPbBr<sub>3</sub>) the lattice is slightly distorted and these Br-Cs distances are split. For small variations in average distances however, changes in the net bonding should also be small.

For the organic ions the situation is quite different. These ions are bonded to Br<sup>-</sup> via the H<sup>+</sup> ions (MA<sup>+</sup> is CH<sub>3</sub>NH<sub>3</sub><sup>+</sup> while FA<sup>+</sup> is the larger, less symmetric, bent molecule, ((NH<sub>2</sub>)<sub>2</sub>CH<sup>+</sup>); if these molecular ions start to rotate or librate [9,16,45–47], the hydrogen bonding will be disrupted for some Br-H pairs (and for full 3D rotations, for all pairs). Consequently, the H-Br bonding will change with  $T$ , and the sharing of charge between Br<sup>-</sup> and H<sup>+</sup> will be reduced when the organic ion is rotating/librating. That in turn allows Br<sup>-</sup> to share more charge with Pb<sup>2+</sup> and the effective Pb-Br bond could be slightly stronger. The  $\sigma^2(T)$  plot for MAPbBr<sub>3</sub> suggests that the MA<sup>+</sup> ion begins to rotate at and above the orthorhombic-tetragonal transition, [16] reducing the bonding between Br<sup>-</sup> and MA<sup>+</sup>, and leading to an increase in  $\kappa$  for the Pb-Br pair above 155 K. Conversely if the organic ion is tethered to the PbBr<sub>3</sub> lattice via a very strong (and shorter) H bond, as proposed by Singh *et al.* [13] for FAPbBr<sub>3</sub>, then the sharing of charge between Br<sup>-</sup> and such H<sup>+</sup> ions would increase. See the Discussion Section for more details.

Lastly we address the bonding and effective spring constant between the Br<sup>-</sup> ion and the Cs<sup>+</sup> ion in CsPbBr<sub>3</sub>. In Fig. 5,  $\sigma^2(T)$  is plotted as a function of  $T$  for the first Cs-Br pair. Also plotted is the cD fit to the data, from which the effective spring constant is calculated using Eq. (3);  $\kappa = 0.89 \text{ eV/\AA}^2$ . This spring constant is significantly weaker (roughly a factor of 2) than that for the Pb-Br pair, consistent with the much longer Cs-Br bond length. The error in  $\sigma^2$  grows rapidly with  $T$  and above 150 K, the EXAFS oscillations are too weak to

get reasonable fits without more averaging. We note too that the static disorder term is small.

### E. Anharmonicity, asymmetry, and $C_3$

An important feature of the perovskites is that the Pb-Br pair distribution function becomes asymmetric [14–16,23] at elevated temperatures as the atoms explore larger regions in phase space with increasing vibration amplitudes. These PDFs are obtained from structural measurements which yield various moments of the distribution, as discussed in Sec. IV B for EXAFS. How such asymmetry is related to the interatomic potential is less clear, particularly if the structure is more complex as in the case when off-center displacements are present. Further, because only a few moments can be measured, the exact shape of the PDF cannot be determined precisely. Note that even for a simple, realistic pair potential, the resulting pair distribution function is intrinsically asymmetric because the atomic forces are slightly different when the bond is compressed compared to when it is extended—a hard core repulsion for very short distances and a weak attractive force for large separations. How asymmetric the PDF is, then depends on how large the displacements are from the potential minimum.

We have obtained the EXAFS asymmetry parameter  $C_3$  for all three materials using nonlinear least squares fits to theoretical FEFF EXAFS functions and plotted them in Fig. 6. Furthermore, as described below and in more detail in Appendices A and B, we derive two new methods to extract  $C_3$  based on the shifts in zero crossing of the  $k$ -space data and the positions of the isosbestic points. These new methods intuitively connect the experimental EXAFS data to the asymmetric Pb-Br PDF and are particularly easy to visualize because of the large asymmetry in these materials.  $C_3$  values obtained with these methods for the Pb  $L_{III}$  edge of MAPbBr<sub>3</sub> are compared to the traditional method in Appendix B. Interested readers will find a full discussion of the derivation and insights these models give in Appendix A and B.

The values of  $C_3$ , obtained from nonlinear least-squared fits using theoretical FEFF7 [40] EXAFS functions, are plotted in Fig. 6.  $C_3$  is much higher in FAPbBr<sub>3</sub> compared to MAPbBr<sub>3</sub>, particularly near 150 K, but is significantly smaller for CsPbBr<sub>3</sub>. The FAPbBr<sub>3</sub> data also indicate a clear change in  $C_3$  at the o-t transition, with  $C_3$  decreasing slightly just above the transition; however at 250 K, the values of  $C_3$  for FAPbBr<sub>3</sub> and MAPbBr<sub>3</sub> are comparable. Although the relative errors for a given temperature (in Fig. 6) are fairly small, systematic errors from the correlation between  $\Delta R$  and  $C_3$  are 10%–15%.

From a fit of the  $C_3$  data to a  $T^2$  dependence, one can then estimate the third-order spring constant,  $k_3$  from the parameter  $A$ , using Eq. (7). In such fits (solid lines in Fig. 6), a small constant off-set was included; i.e.,  $C_3 = A * T^2 + B$  [ $B$  is close to zero: (FA)  $B = 0.8 \times 10^{-4} \text{ \AA}^3$ ; (MA)  $B = 0.5 \times 10^{-4} \text{ \AA}^3$ ; (Cs)  $B = 0.3 \times 10^{-4} \text{ \AA}^3$ ]. For the estimation of  $k_3$ , the corresponding value of  $\kappa$  is needed; for MAPbBr<sub>3</sub> and CsPbBr<sub>3</sub>, we used  $\kappa$  near 300 K while for FAPbBr<sub>3</sub>, the value of  $\kappa$  is for lower  $T$ ,  $\sim 150$  K. For MAPbBr<sub>3</sub>,  $k_3 = -1.6 \text{ eV/\AA}^3$ , for FAPbBr<sub>3</sub> (low  $T$ ),  $k_3 = -6.06 \text{ eV/\AA}^3$ , while CsPbBr<sub>3</sub> has a much smaller value at 250 K,  $k_3 = -0.4 \text{ eV/\AA}^3$ . There are few estimates for  $k_3$  in the literature, but Fornasini *et al.* [48]

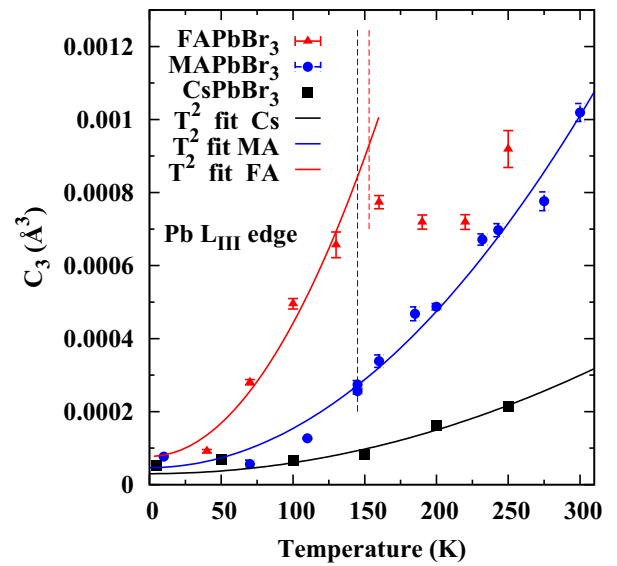


FIG. 6. Comparison of  $C_3(T)$  from least squares fits for FAPbBr<sub>3</sub>, MAPbBr<sub>3</sub>, and CsPbBr<sub>3</sub>, plus fits to a  $T^2$  dependence ( $C_3 = A * T^2 + B$ ). For FAPbBr<sub>3</sub>, because of the break in the curve at the o-t transition, this fit was only from 0 to 150 K. Estimates for  $k_3$  can be obtained from the constant  $A$ . The values of  $C_3(T)$  obtained from the analysis of the shifts of the zero crossings in  $k$  space, gave similar values of  $C_3(T)$ ; these are compared in Ref. [28] (Fig. S8). The colored vertical dotted lines show the position of the o-t transition in FAPbBr<sub>3</sub> and MAPbBr<sub>3</sub>.

give several examples in Table I of their paper. Systems with comparable values of  $\kappa$  are CuCl ( $\kappa = 1.4 \text{ eV/\AA}^2$ ) and  $\beta$ -AgI ( $\kappa = 1.75 \text{ eV/\AA}^2$ ). The corresponding values for  $k_3$  for these two compounds are  $-1.23$  and  $-0.75 \text{ eV/\AA}^3$ , respectively, which are comparable to the values obtained for MAPbBr<sub>3</sub> and CsPbBr<sub>3</sub>; see Table III.

However the above procedure for extracting  $C_3$  in least-squared fits is opaque for most people who are nonexperts in EXAFS. It is not clear from plots of either the  $k$ -space data as in Figs. S1 or S2 in Ref. [28], or from the changes with temperature in  $r$ -space data as shown in Fig. 2, whether or not the asymmetry parameter  $C_3$ , is needed. A useful, intuitive “fingerprint” for determining the presence of a significant asymmetry is found in the  $k$ -space data when multiple back Fourier Transformed (back FT) scans are overlaid as in Fig. 7. We focus on the zero crossings  $k_n$ , where the  $k$ -space function changes sign ( $n$  orders the zero crossings). When the PDF is symmetric, the zero crossings shift very little with increasing temperature, because of the weak temperature dependence of  $r_{\text{avg}}$ ; however if  $C_3$  is significant, there is an accordionlike effect—the shifts of the zero crossings become progressively larger with increasing  $k$  and the magnitude of these shifts grows with temperature. This is shown explicitly in the back FTs for the Pb-Br peak in Fig. 7 for FAPbBr<sub>3</sub>, MAPbBr<sub>3</sub>, and CsPbBr<sub>3</sub>.

It is important to show that  $C_3$  can be obtained from the shifts in the zero crossings in  $k$  space, as detailed in Appendix A; these values are consistent with those shown in Fig. 6 and compared in Fig. S8 in Ref. [28].



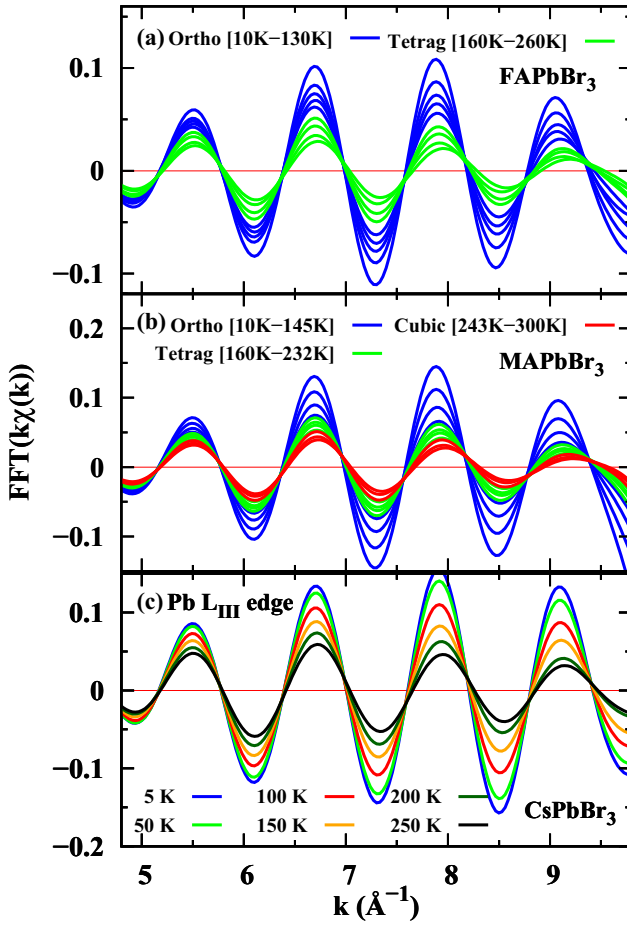


FIG. 7. Expanded view of back Fourier transformed Pb  $L_{III}$  data showing the shifts of the zero crossings at high  $k$ ; these shifts increase with  $T$  for (a) FAPbBr<sub>3</sub>, (b) MAPbBr<sub>3</sub>, and (c) CsPbBr<sub>3</sub>. MAPbBr<sub>3</sub> (b) has the largest shifts near  $9.4 \text{ \AA}^{-1}$  at high  $T$ , while CsPbBr<sub>3</sub> (c) has the smallest shifts.

In addition, a close inspection of the  $k$ -space data just below each zero crossing, shows that there is also an isosbestic point where all curves cross at the same value of  $k = k_{ib,n}$ , independent of temperature, see Appendix B. For these points,  $\chi(k)$  must be independent of temperature, indicating an experimental relationship between amplitude and phase; i.e., there is an equation explicitly relating  $C_3(T)$  to  $\sigma^2(T)$ . This to our knowledge is the first time such a relationship has been shown experimentally. In this analysis, the zero crossings discussed above are also needed; details are provided in Appendix B. The resulting equation is

$$\frac{d(\sigma^2)}{dT} 2\pi \left( \frac{k_n - k_{ib,n}}{k_{n+1} - k_{n-1}} \right) = \frac{2k_{ib,n}}{3} \frac{dC_3}{dT}, \quad (4)$$

which can be used to roughly calculate  $C_3$  using  $d(\sigma^2)/dT$  from the analysis of  $\sigma^2$ , the isosbestic points, and the zero crossings (see Appendix B and figures therein).

If one knows (or assumes) the form of an anharmonic pair potential,  $V(x)$  (here  $x$  is the displacement from the potential minimum at  $r_o$ , i.e.,  $x = r - r_o$ ), then it is straightforward to calculate a PDF, as done recently by Liu *et al.* [23] and Schuck

*et al.* [14]:

$$g(x) = \frac{1}{N} \exp \left[ -\frac{V(x)}{k_B T} \right], \quad (5)$$

where  $N$  is a normalization constant. However from a set of a few experimental moments one cannot invert this procedure to extract a unique potential. Also, in the limit of small displacements, most potentials are well described by the harmonic potential [ $V(x) = \kappa x^2/2$ , where  $\kappa$  is the effective spring constant]. When deviations from a harmonic potential are small, most potentials (Morse, Lennard-Jones, 6-12, etc.) can be expanded [14,23,24] as

$$V(x) = \frac{1}{2}\kappa x^2 + k_3 x^3 + k_4 x^4 \dots, \quad (6)$$

where  $k_3$  and  $k_4$  are the third- and fourth-order spring constants. This expansion is often truncated after the  $x^3$  term which determines the asymmetry or skewness of the PDF. The EXAFS parameter  $C_3$  in Eq. (1) is related to  $k_3$ , and, in the high temperature classical limit,  $C_3$  is given by (note that  $k_3$  is negative) [49,50]:

$$C_3 = -\frac{6k_3}{\kappa^3} (k_B T)^2, \quad C_3 = AT^2, \quad (7)$$

where the constant  $A$  is obtained from a fit of the  $C_3$  results to a  $T^2$  dependence, as shown in Fig. 6.  $k_3$  can then be calculated from  $A$ .

## V. DISCUSSION

### A. Bonding and $\sigma^2$

The temperature dependence of  $\sigma^2(T)$  for the Pb-Br pair provides important information about the Pb-Br bonding in these materials. The results for FAPbBr<sub>3</sub> and CsPbBr<sub>3</sub> are of comparable magnitude to our earlier study on MAPbBr<sub>3</sub> [16]. The effective Pb-Br spring constants extracted from fits to the data [see Eq. (3)] for the three materials (Fig. 4), all have similar magnitudes and are comparable to the Pb-X spring constants obtained for other lead-halide perovskites [23].

An important difference between MAPbBr<sub>3</sub> and FAPbBr<sub>3</sub> for  $T \leq 300$  K, is that we observe changes in the Pb-Br bonding strength that occur at the o-t phase transition. For CsPbBr<sub>3</sub>, the o-t transition is above the range of our measurements, near 360 K, and we cannot determine whether a similar change in  $\sigma^2(T)$  occurs. For MAPbBr<sub>3</sub> and FAPbBr<sub>3</sub>, the slope of  $\sigma^2(T)$ , and therefore the effective spring constant,  $\kappa$ , changes at this transition. As noted in our earlier paper [16],  $\kappa$  increases by  $\approx 26\%$  for MAPbBr<sub>3</sub> at the transition (from  $1.43$  to  $1.87 \text{ eV/\AA}^2$ ), and other structural properties (diffraction bond lengths, longitudinal correlated motion, etc.) were consistent with such an increase in  $\kappa$ . For FAPbBr<sub>3</sub>, the effect is reversed and the magnitude of the change is larger—the slope of  $\sigma^2(T)$  increases significantly and the Pb-Br spring constant decreases by roughly 60% above the o-t transition. This indicates that the distribution of shared charge between Br<sup>-</sup> and the two positive ions (Pb<sup>+2</sup>, and either MA<sup>+</sup> or FA<sup>+</sup>), changes in a different way for the two molecular cations.

For FAPbBr<sub>3</sub>, Singh *et al.* [13] report, based on MD simulations, that at 300 K (cubic phase) one H<sup>+</sup> ion on the FA ion sticks to one of the 12 neighboring Br<sup>-</sup> ions 91% of the time, via a very strong H bond; the bond length is

very short and fluctuates between roughly 1.75 and 2.25 Å over times of order 5 ps (see Fig. 4(b) in Ref. [13]). As a result, the FA<sup>+</sup> molecular ion is tethered to that Br<sup>−</sup> ion and locally the FA<sup>+</sup> center-of-mass is shifted off-center. Since the off-center directions are randomly distributed over all the sites, the average position of the center of mass will be at the center of the site, much as occurs for displaced atoms in an order-disorder ferroelectric system above the ferroelectric transition temperature (in the paraelectric phase).

Franz *et al.* [11] have recently studied FAPbBr<sub>3</sub> using neutron diffraction and concluded that at 300 K, the FA molecule was on average, at the center of the A site. Thus their results are consistent with Singh *et al.* [13].

In contrast to FAPbBr<sub>3</sub>, the shortest H-Br bonds in the cubic phase of MAPbBr<sub>3</sub> are much longer—roughly 2.5 Å, and rarely are shorter than 2.0 Å [16]; the H-Br bonds are rapidly forming and breaking on picosecond timescales (see Fig. S19 in SI, Ref. [16]). On average there are two H-Br bonds formed with two different MA<sup>+</sup> cations—but the MA<sup>+</sup> cations that are bonded to a particular Br<sup>−</sup> ion change rapidly over time.

When H<sup>+</sup> forms a very strong bond with Br<sup>−</sup> then the sharing of charge between these two ions increases and sharing of charge for that Br<sup>−</sup> ion with Pb<sup>2+</sup> would decrease. However, for FAPbBr<sub>3</sub>, it appears that at a given instance in time not all Br<sup>−</sup> ions are bonded to a H<sup>+</sup> ion and then an average over configurations is needed. If the effects when strong H<sup>+</sup>-Br<sup>−</sup> bonds have formed dominate, then the sharing of charge between Br<sup>−</sup> and Pb<sup>2+</sup> could decrease on average, the Pb-Br bond strength would then be slightly weaker, and correspondingly, the value of  $\kappa$  for Pb-Br in FAPbBr<sub>3</sub> above the transition would be smaller. This is what we observe.

The structures on the absorption edges in the XANES (x-ray absorption near edge structure) plots for the Br K and Pb L<sub>III</sub> edges, provide another probe of changes in the electron distributions on these atoms. For the Br K edge, the XANES for FAPbBr<sub>3</sub> (SM Fig. S11b) are very similar to that observed for MAPbBr<sub>3</sub> (see Figs. S11 and S12 in SI for Ref. [16]); however the temperature dependence for the amplitude of the first peak is different for the two systems. For MAPbBr<sub>3</sub> the amplitude of the first peak in the XANES (near 13 478 eV) changes monotonically with  $T$ , with no structure at the o-t transition (Fig. S13, in SI for Ref. [16]). In contrast, the amplitude of this Br XANES peak for FAPbBr<sub>3</sub> shows a significant drop above the o-t transition (see Fig. S12(b) in Ref. [28]).

For the Pb L<sub>III</sub> XANES however, the overall behavior is different in the two systems. The second peak in the Pb XANES for MAPbBr<sub>3</sub> (see Fig. S12 in SI for Ref. [16]) is much larger than the first peak, while for FAPbBr<sub>3</sub> the amplitudes of these two peaks are comparable. Also, the amplitude of the first two peaks in the Pb L<sub>III</sub> XANES of MAPbBr<sub>3</sub> show changes that correlate with the o-t transition, while no anomaly is observed at this o-t transition for FAPbBr<sub>3</sub> (see Ref. [28] Fig. S12(a)).

It is clear that the nature of the A-site cation inside the PbBr<sub>3</sub> cage has a significant influence on the structure of the halide perovskite. In the orthorhombic phase, the volume of the unit cell increases slightly, by  $\approx 6\%$  from CsPbBr<sub>3</sub> to MAPbBr<sub>3</sub> to FAPbBr<sub>3</sub>. However, there is a much larger change in the size of the A-site cations—Ghosh *et al.* [51] give the ionic radii for Cs<sup>+</sup>, MA<sup>+</sup>, and FA<sup>+</sup> as 1.67, 2.17,

and 2.53 Å, a roughly 50% increase from Cs<sup>+</sup> to FA<sup>+</sup>. In addition, the ion symmetry changes as the FA<sup>+</sup> cation is bent; this larger size and bent nature of FA<sup>+</sup> will hinder rotations within the PbBr<sub>3</sub> cage (because the volume swept out in rotation is larger). Whereas there is clear evidence that MA<sup>+</sup> begins to librate or rotation at temperatures well below the orthorhombic-tetragonal transition and even below 100 K [9,16,45–47], the motion of FA<sup>+</sup> is more restricted [13,52], Singh *et al.* [13] report from molecular dynamics simulations that at 300 K (cubic phase), the FA<sup>+</sup> cation is shifted off-center (in random directions) and one end of the molecular ion bonds to the PbBr<sub>3</sub> lattice for a large fraction of time, via short Br<sup>−</sup>-H<sup>+</sup> bonds. It is not clear if the FA<sup>+</sup> cation remains off-center in the lower temperature phases. The XANES for Pb and Br edges do show small but significant changes with  $T$ , indicating slight re-distributions of charge, some of which are correlated with the o-t transition, and hence are consistent with small changes in  $\kappa$ .

At the tetragonal-cubic (t-c) phase transition in MAPbBr<sub>3</sub> (near 235 K), there is no equivalent break in the slope of  $\sigma^2$  to that for the o-t transition. The equivalent t-c transition in FAPbBr<sub>3</sub> occurs near 266 K [10]; unfortunately our data set for FAPbBr<sub>3</sub> does not go above 250 K. However, the value of  $\sigma^2$  at 300 K for the Pb-Br pair in FAPbBr<sub>3</sub> from Singh *et al.* [13] (see Fig. 4) is consistent with our data within errors. Note that the errors in  $\sigma^2$  grow rapidly with  $T$  as the damped amplitude of the high  $k$ -range data approaches the noise level at high temperatures. Consequently very high-quality data would be needed to check for a possible break at 266 K in FAPbBr<sub>3</sub>.

## B. Asymmetry and pair potential anharmonicity for Pb-Br

Below, we discuss and compare different models used to explain asymmetry in the PDFs for the nearest-neighbor Pb-Br pair of lead halide perovskites. Four asymmetric models are constructed, and the cumulants extracted for each distribution (see Sec. VI in Ref. [28]), are compared, along with those obtained from fits of the EXAFS equation. Ultimately, we find that single-site asymmetric PDF models such as those derived from single-site anharmonic potentials, are the best descriptor for the Pb-Br PDF.

At low temperatures, the Pb-Br pair potentials can be approximated as harmonic with the corresponding pair distributions well-described by Gaussian functions. At higher temperatures, the harmonic approximation is no longer valid due to finite temperature explorations of the anharmonic pair potential. As a result, the Gaussian distribution is no longer a sufficient model and deviations from it must be parameterized. In this section, we compare and discuss four different approaches that can be used to model asymmetry/anharmonicity in slightly disordered materials such as the lead bromide perovskites. Although the models are quite different, the PDF's they generate are very similar, in part because the deviations from a Gaussian are still small for  $T < 300$  K.

Consequently, the exact shape of the distribution function cannot be determined precisely; for each model a set of parameters, obtained in fits of the data, define the shape of a PDF. In most cases the quantities that can be directly extracted from the data analysis are the moments of the distributions

about  $r_{\text{avg}}$ ,  $M_n = \langle (r - r_{\text{avg}})^n \rangle$ ; one expansion in terms of these moments is the cumulant expansion [36], and the parameters are referred to as the cumulants—see Sec. IV B. Note that different distribution models can have similar cumulants. Consequently a given PDF model may not be unique; however the cumulants are model independent.

For a general (non-Gaussian) distribution, we use the same notation for the first two cumulants as used for Gaussian functions:  $r_{\text{avg}}$  is the first cumulant (first moment) and  $\sigma^2$  is the second cumulant (second moment relative to  $r_{\text{avg}}$ ). To these we add  $C_3$  (skewness) and  $C_4$  (kurtosis), both of which are zero for a Gaussian distribution.

For the APbBr<sub>3</sub> perovskites, the asymmetry parameter,  $C_3$ , is large enough to produce an observable shift in the zero crossing of the  $k$ -space data, even at temperatures of order 150 K, as shown in Fig. 7 for the Pb-Br peak. These shifts are plotted and discussed in Appendix A. Such large asymmetries can arise for example, from an anharmonic interatomic pair potential which constrains the distribution of thermal excursions of both atoms in the atomic pair and hence the PDF [36]. The asymmetry of the PDF increases with temperature for such an anharmonic potential as the vibration amplitude increases, particularly in the tetragonal and cubic phases for the APbBr<sub>3</sub> perovskites. One approach used for these systems is to assume a Morse potential [14,23] which has three parameters; these parameters will determine the average bond length, and the second and third moments,  $\sigma^2$  and  $C_3$ .  $C_4$  will be some combination of these potential parameters but cannot be determined independently for this form of the potential.

An alternative approach is to assume some model of an asymmetric pair distribution function [38] and vary the associated parameters to fit the data. For these perovskites, some have postulated that the Pb atom is displaced off-center along a  $\langle 111 \rangle$  direction [15], but along randomly chosen axes throughout the crystal (similar to a displacive ferroelectric above the transition temperature). Assuming this is quasistatic on phonon timescales, then locally the Pb atom has three nearer Br neighbors and three slightly more distant Br neighbors— independent of the choice of the  $\langle 111 \rangle$  off-center direction. This can be modeled as a split peak, i.e., a sum of two Gaussians with slightly different bond lengths ( $r_1 < r_2$ ) and different  $\sigma$ 's ( $\sigma_1 < \sigma_2$ ). For suitable choices of the splitting and  $\sigma$ 's, the distribution is asymmetric.

Both models (anharmonic potential and split peak distribution) have been applied to the PDFs for the lead halide perovskites but no researchers have used both models and then compared the results—we will do so here.

First, to demonstrate the nonuniqueness of asymmetric pair distribution functions, we construct four separate PDFs to describe the nearest neighbor Pb-Br peak in the  $r$ -space data for MAPbBr<sub>3</sub> at 300 K; this data set has the best S/N at high  $T$ . The four models are: 1) the  $\Gamma$  function-based PDF that is intrinsically asymmetric (3 parameters, which define  $r_{\text{avg}}$ ,  $\sigma^2$  and  $C_3$ ) described by Yang *et al.* [38], 2) a split pair of Gaussians using parameters obtained from a fit of the 300 K EXAFS data to this model (4 parameters, but only 3 independent, as the small splitting is fixed to that of Laurita *et al.* [15] for MAPbBr<sub>3</sub>), 3) a PDF based on an anharmonic Morse potential as used by Liu *et al.* [23] and Schuck *et al.* [14] for iodide perovskites (again 3 parameters,  $r_o$ ,  $G$ , and

$\alpha$ ); however a high temperature approximation [based on an expansion—see Eq. (6)] can be written in terms of more useful parameters ( $r_1$ ,  $\sigma^2$ , and  $C$  See Eq. S15 in Ref. [28]), and 4) another asymmetric PDF similar to those used for amorphous materials in which the  $r$ -dependence of the PDF is different above and below the peak. [53] A simple example of this type of PDF is formed using different exponentials above and below the peak, i.e., two half-Gaussians with different  $\sigma$ 's and a different normalization (3 parameters,  $r_o$ ,  $\sigma_1$ , and  $\sigma_2$ )—see Ref. [28] for more details. In each case there are 3 independent parameters and that allows three independent quantities to be adjusted  $r_{\text{avg}}$ ,  $\sigma_{\text{avg}}^2$ , and  $C_3$ . The cumulants can also be calculated analytically for the  $\Gamma$  function and the split pair distributions; definitions of the parameters and more details are provided in Ref. [28]. An important constraint for the split peak model is that to have  $C_3$  increase as  $T^2$ , requires that the splitting increase linearly with  $T$  - see Eq. S10 in Ref. [28].

We have fit the EXAFS data directly to the EXAFS equation [Eq. (1), initially adding only the  $C_3$  parameter], and also to two different asymmetric PDF models—the asymmetric  $\Gamma$  function and the split peak model. The goodness-of-fit parameters in these fits are comparable for these three-parameter fits, and cannot be used to differentiate between the two PDF models. However, a difference between models can be obtained by including  $C_4$  in fits of MAPbBr<sub>3</sub> at 300 K using the EXAFS equation, and comparing this value of  $C_4$  with the calculated values for the two PDFs ( $\Gamma$  function and split peak distributions). Including  $C_4$  for fits using the EXAFS equation at 300 K improves the fit and is considered a significant improvement based on the Hamilton F-test [54]. The fits including  $C_4$  are discussed in more details below.

For the PDF based on a Morse potential (No. 3) we have adjusted the parameters  $r_1$ ,  $\sigma^2$ , and  $C$  (Eq. (S15) in Ref. [28]) to make the first three cumulants close to the results for fits to the EXAFS equation; here  $C$  directly controls  $C_3$ . Similarly we adjusted the parameters for the two half-Gaussian model (No. 4) so that  $r_{\text{avg}}$  and  $\sigma^2$  agree with the fits to the EXAFS equation. In this case no parameter directly controls  $C_3$ , and it depends sensitively on all three parameters:  $r_o$ ,  $\sigma_1$ , and  $\sigma_2$ . Small changes in these parameters can lead to a large variation in  $C_3$ .

The four distributions discussed above are plotted in Fig. 8; see Table II for the parameters  $r_{\text{avg}}$ ,  $\sigma^2$ ,  $C_3$ , and  $C_4$ . The cumulants were determined for each distribution by numerically calculating the first four moments of each model (see Sec. VII in Ref. [28]). The specific parameters for MAPbBr<sub>3</sub> are given in Ref. [28] for these models at 300 K. The calculated values of the first three cumulants are all quite similar although the  $C_3$  values for the two Gaussian model and the two half-Gaussian model are a bit low. However, the  $C_4$  values (fourth moment) have large variations between models and thus provide additional constraints. Experimentally for MAPbBr<sub>3</sub>,  $C_4$  is positive above 200 K (see Fig. S13 in Ref. [28]), indicating a slight sharpening of the PDF near the center of the distribution and expansion in the tails; at 300 K,  $C_4$  is  $\approx 10.4 \times 10^{-5} \text{ \AA}^{-4}$  from fits to the EXAFS equation [Eq. (1)]. In Table II the  $C_4$  value for the Morse potential is the highest while that for the  $\Gamma$  function is closest to the result from a fit to the EXAFS



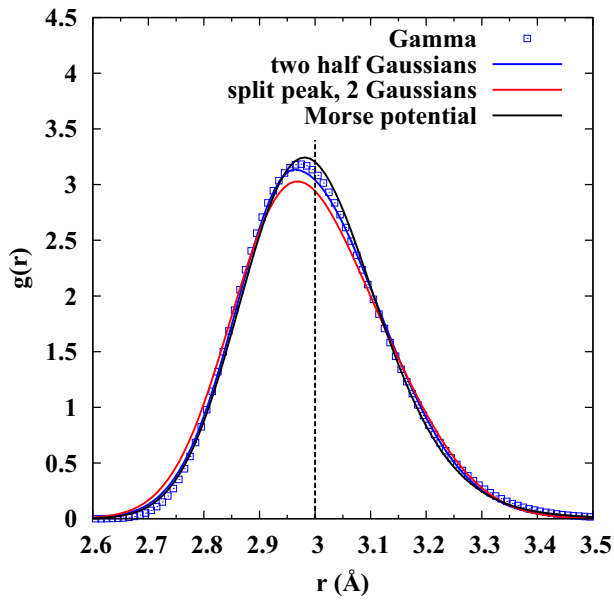


FIG. 8. The four pair distribution functions used to describe the 300 K Pb-Br peak in the EXAFS data for MAPbBr<sub>3</sub>. Note that the average Pb-Br bond length,  $r_{\text{avg}}$  (dotted vertical line), is above the maximum of the distribution function. The cumulants are tabulated in Table II, and the equations and parameters used to calculate these distributions are provided in Ref. [28]. Note the slightly different shapes for the various distributions.

equation. In contrast,  $C_4$  for the two Gaussian, split-site model 2, is negative which suggests a flattened distribution instead of a sharpened one. Note that a flattened distribution is expected if the two Gaussians are sufficiently split. In addition, the analytic expressions for the cumulants for this model, given in Ref. [28] [Eq. (S10)], show this explicitly. Whereas  $C_3$  is proportional to the splitting parameter  $D$  [ $D = 0.5(r_2 - r_1)$ ] and  $D^2$  additively contributes to  $\sigma_{\text{avg}}^2$ ,  $C_4$  is the difference between a term in  $\sigma^4$  and  $D^4$  [Eq. (S10)], and a larger value for  $D$  leads to a reduction in and eventually a negative value for  $C_4$ . The cross-over (for which  $C_4$  is  $\approx 0$ ) is near  $2D = 0.115 \text{ \AA}$ , which is shorter than the splitting reported by Laurita *et al.* [15],  $\approx 0.14 \text{ \AA}$ . Decreasing the splitting to  $0.115 \text{ \AA}$  at 300 K, for the 2-Gaussian model also makes the fit to the EXAFS data

TABLE II. Summary of cumulants obtained for the EXAFS equation and for four specific PDF's representing the asymmetric Pb-Br pair distribution function at 300 K.  $C_4$  is particularly sensitive to the low and high  $r$  tails of the distribution in the moment integrals, in part because it is the difference between two comparable numbers [related to the 4th moment and the second moment squared—see Ref. [28] Sec. VII and Eq. (S17)]. Error estimates for last digit are are given in the parenthesis.

Model	$r_{\text{avg}}(\text{\AA})$	$\sigma^2(\text{\AA}^2)$	$C_3(10^{-4} \text{\AA}^3)$	$C_4(10^{-5} \text{\AA}^4)$
EXAFS Eq.	2.999(3)	0.016(1)	11(1)	10(2)
Gamma Function	3.002(3)	0.016(1)	10(1)	10(2)
Two Gaussians	2.998(3)	0.017(1)	5.2(6)	-2.9(6)
Morse potential	2.999(3)	0.016(1)	10(1)	17(3)
2 Half-Gaussians	2.999(3)	0.016(1)	6(4)	2.5(5)

much worse. Similarly making  $\sigma_2$  10% larger (which would also increase  $C_3$ ) also makes the goodness-of-fit parameter worse by a factor of 4.

The relatively large positive value for  $C_4$  at 300 K from the EXAFS data fit for MAPbBr<sub>3</sub> (and for several other systems see Fig. S13 in Ref. [28]), compared to the negative value for  $C_4$  obtained for the two Gaussian model, indicates that a split peak model is a poorer model to describe these systems than a Morse potential or some other asymmetric pair distributions such as the  $\Gamma$ -function distribution.

## VI. SUMMARY

The detailed local structure comparisons of the APbBr<sub>3</sub> perovskites show some similarities but also significant differences. Below 300 K, the thermal behavior for the Pb-Br pair in CsPbBr<sub>3</sub> is typical of many solids—the Debye-Waller factor,  $\sigma^2$ , increases smoothly with temperature; it is a constant at low temperatures and becomes linear at higher  $T$ . Also, the static disorder of the Pb-Br bond is very small for CsPbBr<sub>3</sub> but increases with the size of the  $A$ -site cation. More importantly, for the MA<sup>+</sup> and FA<sup>+</sup> cations, the  $T$  dependence of  $\sigma^2$  does not follow an Einstein or correlated Debye model as is observed for most solids; there is a break in  $\sigma^2(T)$  at the orthorhombic-tetragonal (o-t) transition, indicating a small change in effective spring constant  $\kappa$  for the Pb-Br bond. Although the values of  $\kappa$  are comparable for all three systems, ranging from 1.2 to 1.95 eV/ $\text{\AA}^2$ —see Fig. 4, the differences are significant for the MA<sup>+</sup> and FA<sup>+</sup> cations, with a decrease in  $\kappa$  at high  $T$  for FAPbBr<sub>3</sub>, but an increase for MAPbBr<sub>3</sub>. This change at the o-t transition and corresponding small changes in the XANES suggests small redistributions of charge at the o-t transition, which we suggest is related to a difference in the H<sup>+</sup>-Br<sup>-</sup> bonding between the two systems; for MAPbBr<sub>3</sub> the rapid rotations of the MA<sup>+</sup> ion makes these bonds weaker on average. In contrast, a H<sup>+</sup> atom is strongly bonded to Br<sup>-</sup> (very short bond) in FAPbBr<sub>3</sub> and the FA<sup>+</sup> motion is more restricted. Measurements at the Cs  $K$  edge show that the effective spring constant between Cs and Br is much weaker than the Pb-Br spring constant.

The asymmetry parameter  $C_3$  for the Pb-Br pair is also different; there is no obvious break at the o-t transition for MAPbBr<sub>3</sub> but a small decrease at and above the o-t transition for the FAPbBr<sub>3</sub> system. Below 150K,  $C_3$  is largest for FAPbBr<sub>3</sub> and smallest for CsPbBr<sub>3</sub>. Finally at 250–300 K the kurtosis parameter,  $C_4$  becomes significant and is positive for all three systems indicating a slight sharpening at the center of the distribution and a broadening in the wings. A positive value for  $C_4$  is inconsistent with a split-site model for an off-center Pb atom, when the splitting is significant.

Lastly we collect a number of parameters for the Pb  $L_{\text{III}}$  edge analysis together in Table III. Here we have also added a parameter that is a measure of the local “static disorder,” defined as  $\sqrt{\sigma_{\text{static}}^2}$ , and the value of the zero-point-motion static disorder increases systematically as the cation size increases from Cs<sup>+</sup> to MA<sup>+</sup> to FA<sup>+</sup>; see also Fig. S5 in Ref. [28]. Similarly, the extent of asymmetry in the PDF, as captured by  $k_3$  in Table III, increases significantly as the cation size



TABLE III. Collection of parameters (Pb  $L_{III}$  edge) for correlated Debye fits of  $\sigma^2(T)$  and fits of  $C_3$  to  $AT^2 + B$ , for respective compounds.  $k_3$  is calculated from  $A$  using Eq. (7) [ $k_3 = (-Ak^3)/(6k_B)$ ]. For the correlated Debye fits the temperature range for the FAPbBr<sub>3</sub> and MAPbBr<sub>3</sub> data was restricted to  $T$  below the o-t transition or above it; For CsPbBr<sub>3</sub> data, the full temperature range was used. For fits of  $C_3$  to  $AT^2 + B$ , the full temperature range was used for MAPbBr<sub>3</sub> and CsPbBr<sub>3</sub>, but for FAPbBr<sub>3</sub> the  $T$  range was 5–150 K. In calculating  $k_3$  The high temperature spring constants were used for MAPbBr<sub>3</sub> and CsPbBr<sub>3</sub> while the low temperature spring constant was used for FAPbBr<sub>3</sub>. Also included for comparison purposes are the value of  $\sigma_{\text{static}}^2$  (see Eq. (2) and Eq. (S1) of Ref. [28]), the static disorder defined as  $\sqrt{\sigma_{\text{static}}^2}$ , and the value of the zero-point-motion contribution to  $\sigma^2$ . The latter is the value of  $\sigma^2$  at  $T = 0$  when  $\sigma_{\text{static}}^2$  is zero. In the last column, we list the ionic radii of the three ions for comparison purposes (from Ghosh *et al.* [51]).

	Debye fit range (K)	Spring constant (eV/Å <sup>2</sup> )	Debye temp. (K)	$\sigma_{\text{static}}^2$ (10 <sup>-4</sup> Å <sup>2</sup> )	Static Disorder (Å)	Zero point motion (10 <sup>-4</sup> Å <sup>2</sup> )	$k_3$ (eV/Å <sup>3</sup> )	A-site ionic radii (Å)
FAPbBr <sub>3</sub>								
Low Temp.	40–130	1.95(2)	180(7)	45(3)	0.067(2)	27(1)	-6.1(9)	2.53
High Temp.	160–250	1.20(2)	141(5)	7(9)	0.026(2)	34(1)		
MAPbBr <sub>3</sub>								
Low Temp.	10–145	1.43(2)	147(4)	3.5(5)	0.019(1)	30(1)	-1.6(1)	2.17
High Temp.	145–300	1.87(2)	167(4)	23(7)	0.047(3)	26(1)		
CsPbBr <sub>3</sub>								
Full Range	5–250	1.82(2)	165(4)	1.9(6)	0.014(2)	25(1)	-0.41(5)	1.67

increases. In contrast, the Pb-Br spring constant for all the cations are roughly the same and do not appear to exhibit a trend as a function of cation size. Finally there appears to be an anomaly in  $\sigma^2(T)$  at very low  $T$  for FAPbBr<sub>3</sub>; the lowest points are not close to the correlated Debye fit, and suggest some other mechanism is active in FAPbBr<sub>3</sub> in the orthorhombic phase (Figs. S3 and S5 in Ref. [28]).

### ACKNOWLEDGMENTS

The EXAFS experiments were performed at the Stanford Synchrotron Radiation Lightsource (SSRL), which is supported by the U.S. Department of Energy, Office of Science, Office of Basic Energy Sciences under Contract No. DE-AC02-76SF00515. We thank David Cahen for suggesting these measurements and G. Bunker for helpful discussions about the gamma function distribution function. This work (conceptualization, XRD, interpretation) is supported by the Center for Hybrid Organic Inorganic Semiconductors for Energy (CHOISE), an Energy Frontier Research Center funded by the Office of Basic Energy Sciences, an office of science within the US Department of Energy (DOE). HIK acknowledges funding through the Department of Energy (DOE), Office of Basic Energy Sciences, Division of Materials Sciences and Engineering, under contract DE-AC02-76SF0051 (single crystal synthesis). J. A. V. acknowledges fellowship support from the Stanford University Office of the Vice Provost of Graduate Education and the National Science Foundation Graduate Research Fellowship Program under Grant No. DGE 1656518. Part of this work (single crystal x-ray diffraction) was performed at the Stanford Nano Shared Facilities, supported by the National Science Foundation, Division ECCS-2026822, Grant No. NSF-2026822.

### APPENDIX A: EXTRACTING $C_3$ FROM ZERO-CROSSINGS

As noted in Fig. 7, the zero crossings in  $k$ -space shift to higher  $k$ , both with increasing  $k$  and with increasing  $T$ ; we find this a more intuitive way of visualizing  $C_3$  effects. To our

knowledge, this is a new approach; extracting  $C_3$  from these shifts has not been done before.

It is important to recognize that in EXAFS  $k$ -space plots, an asymmetric pair distribution function that is larger on the high- $r$  side, leads to a shift of the zero crossings to *higher*  $k$ , relative to a symmetric distribution. The data at 10 K for which the PDF is close to symmetric, serves as this reference point. This shift of the zero crossings for an asymmetric PDF is explained in more detail in Ref. [28]—see Fig. S9.

In Fig. 9, the relative shifts at each zero crossing are plotted for the Pb-Br pair in the Pb  $L_{III}$  data for FAPbBr<sub>3</sub>, MAPbBr<sub>3</sub>, and CsPbBr<sub>3</sub>, as a function of  $k$  for each temperature. The relative shifts  $\Delta k_n(T)$  are defined as

$$\Delta k_n = k_n(T) - k_{n,0}(10 \text{ K}). \quad (\text{A1})$$

Here  $k_n(T)$  is the  $n$ th zero crossing at temperature  $T$ . At a fixed  $T$ , the curvatures of these functions, plotted as a function of  $k$  in Fig. 9, provide direct evidence that  $C_3$  is significant. Note that in CsPbBr<sub>3</sub>,  $C_3$  is clearly smaller than in FAPbBr<sub>3</sub> and MAPbBr<sub>3</sub> (see Figs. 9 and 6). Also, the signal-to-noise for the FAPbBr<sub>3</sub> sample was poorer and there is more scatter in the zero crossing values.

To model this behavior, consider the phase  $\Theta$  of the sine function in the EXAFS equation [Eq. (1)], given by

$$\Theta = 2kr - \frac{4}{3}C_3k^3 + \Phi(k). \quad (\text{A2})$$

Here  $\Phi(k)$  is a  $T$ -independent phase from the excited and backscattering atoms and it is assumed that  $C_3$  is  $\sim 0$  at low  $T$ . [Note there is also another approach that uses the difference in  $\Theta$ , i.e.,  $\Theta(T) - \Theta(10 \text{ K})$ . This is discussed in Ref. [28]—see Figs. S6 and S7. At a particular zero crossing,  $\Theta$  remains constant. We first define  $r_{\text{avg}}(T) = r_{\text{avg}}(10 \text{ K}) + \Delta R(T)$ ,  $k_n(T) = k_{n,0}(10 \text{ K}) + \Delta k_n(T)$  and approximate  $k_n^3(T)$  to first order as  $k_{n,0}^3(10 \text{ K}) + 3\Delta k_n(T)k_{n,0}^2(10 \text{ K})$ . Then  $\Delta k_n(T)$  can be written as a function of  $\Delta R$  and  $C_3$ :

$$\Delta k_n = \frac{\frac{2}{3}C_3k_{n,0}^3/r_{\text{avg}} - \Delta Rk_{n,0}/r_{\text{avg}}}{1 - 2C_3k_{n,0}^2/r_{\text{avg}}}. \quad (\text{A3})$$

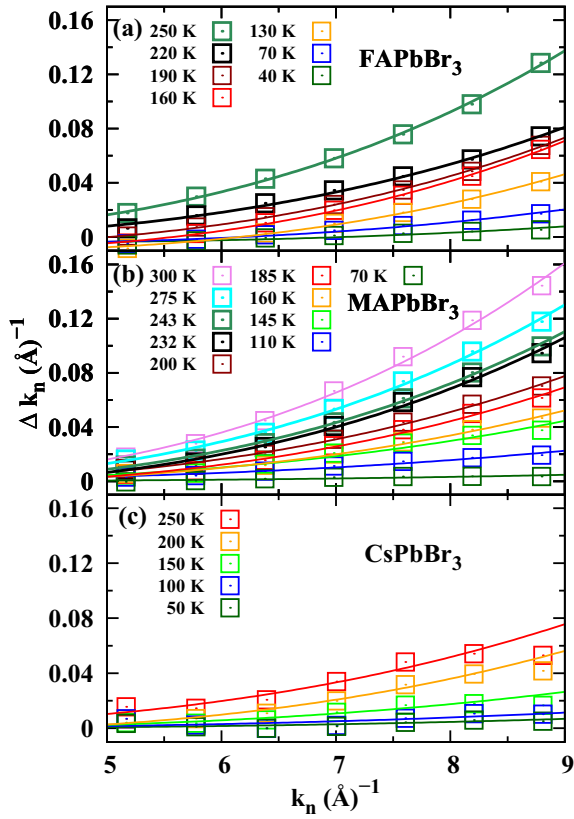


FIG. 9. Plots of the shifts of the zero crossings as a function of  $k_n$  for each temperature at the Pb  $L_{III}$  edge for (a) FAPbBr<sub>3</sub>, (b) MAPbBr<sub>3</sub>, and (c) CsPbBr<sub>3</sub>. The lines are fits to the model discussed in the text [Eq. (A3)], with  $\Delta R$  and  $C_3$  as fitting parameters. y-axis scales are the same for comparison, but note that FAPbBr<sub>3</sub> and CsPbBr<sub>3</sub> only have data up to 250 K.

Equation (A3) shows explicitly the positive correlation between  $\Delta R$  and  $C_3$ ; a small increase in  $\Delta R$  can be partially compensated by an increase in  $C_3$ , leading to a very small change in  $\Delta k_n(T)$ .

At each temperature, the data (points in Fig. 9) are fit to Eq. (A3) using the parameters  $\Delta R$  and  $C_3$ . These fits are shown as lines on Fig. 9, and model the zero crossing data well. Note that this analysis is independent of the theoretical quantities calculated by FEFF7 [40].

#### APPENDIX B: ISOSBESTIC POINTS AND $\sigma^2$ - $C_3$ RELATIONSHIP

As noted earlier (see Fig. 7) there are also isosbestic points at values of  $k$ ,  $k_{ib,n}$ , just below the  $n$ th zero crossings in the Pb $L_{III}$  back Fourier transformed data; the corresponding back Fourier transformed data for the Br  $K$  edge in MAPbBr<sub>3</sub> are shown in Fig. 10. On this enlarged scale, the isosbestic points are clearly visible just below each zero crossing; note that both the isosbestic points and the positions of the zero crossings are shifted compared to those for the Pb  $L_{III}$  edge, because the atomic phases for the Pb  $L_{III}$  and Br  $K$  edges are different.

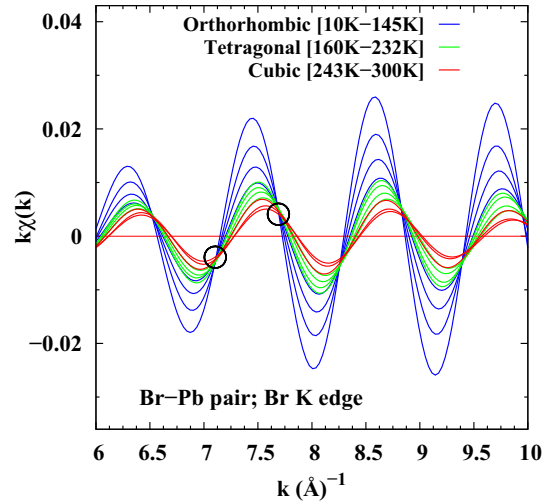


FIG. 10. Back Fourier Transformed data for the Br-Pb pair in MAPbBr<sub>3</sub> at the Br  $K$  edge. Six isosbestic points are visible between 6.5 and 9.5  $\text{\AA}^{-1}$  (see black circles for examples near 7 and 7.6  $\text{\AA}^{-1}$ ), where  $d\chi/dT = 0$ . These points are shifted compared to the equivalent points in Fig. 7 for the Pb  $L_{III}$  edge but can also be used in the analysis described below.

These isosbestic points together with the zero crossings, provide a relationship between the amplitude of  $\chi$  and its phase, as a function of temperature. This provides another new way to determine  $C_3$  and hence connect to the PDF asymmetry; it also provides an experimental connection between  $\sigma^2$  and  $C_3$ , that to our knowledge has not been utilized before to obtain  $C_3$ .

The shift in phase between the isosbestic point and the corresponding zero crossing (i.e.  $\Theta(k_n) - \Theta(k_{ib,n}) = \delta\Theta_n$ ) is small. Also, the value of  $\chi$  is small and changes sign from one isosbestic point to the next. At these special points in  $k$ -space,  $\chi$  is independent of temperature, i.e.,  $d\chi/dT = 0$ , and that gives an experimental relationship between  $\sigma^2$  and  $C_3$ . Starting with Eq. (1) and ignoring  $C_4$  and the weak temperature dependence of  $r$ , we can write for the Pb-Br (or Br-Pb) pair:

$$k\chi(k, r) = A_o \exp(-2\sigma^2 k^2) \sin\left(2kr - \frac{4}{3}C_3 k^3 + \phi(k)\right),$$

$$A_o = \frac{NS_0^2}{r^2} F(\pi, k) e^{-2r/\lambda(k)}, \quad (\text{B1})$$

where the quantities in  $A_o$  are essentially independent of T. Then setting  $d\chi/dT = 0$  yields

$$A_o[\exp(-2\sigma^2 k^2)] \times \left(2k^2 \frac{d(\sigma^2)}{dT} \sin \Theta(k_{ib,n}) + \frac{4}{3} \frac{dC_3}{dT} k^3 \cos \Theta(k_{ib,n})\right) = 0. \quad (\text{B2})$$

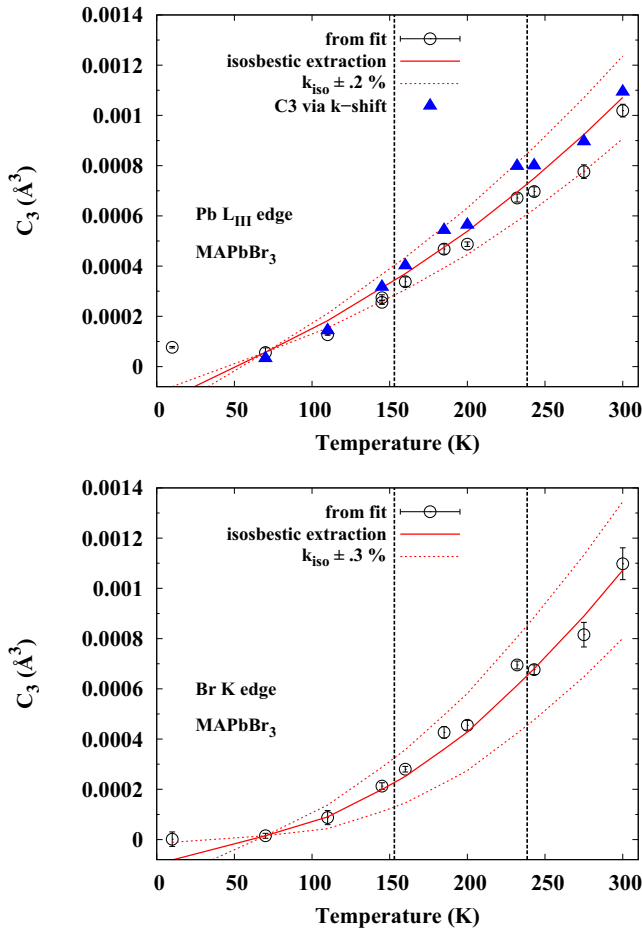


FIG. 11. (a) Comparison of  $C_3$  values for MAPbBr<sub>3</sub> obtained from least squares fitting of data (open circles) and numerically integrating Eq. (B4) using the isosbestic points, the measured zero crossings and the fits to  $\sigma^2(T)$ —red solid line. Because there is some uncertainty in the values of  $k_{ib,n}$  we also plot (dotted red lines) the results with  $k_{ib,n}$  varied by  $\pm 0.2\%$ . For comparison we have also plotted the  $C_3$  values obtained from the zero crossings (Appendix A) (filled triangles). (b) Similar results for  $C_3$  at the Br K edge; here, because the Br K edge data have more noise, we considered 0.3% variations in  $k_{ib,n}$ . The results for the numerical integrations were normalized to the results from the least squares fits at 70 K. Vertical dotted black lines show the phase transition temperatures.

Note also that when  $\sin \Theta(k_{ib,n})$  is slightly positive,  $\cos \Theta(k_{ib,n})$  is negative, and vice versa. Finally, because  $k_{ib,n}$  is very close to a zero crossing,  $\cos \Theta(k_{ib,n}) = \pm 1$ , and in the small angle approximation,

$$\sin \Theta(k_{ib,n}) = \sin(n\pi - \delta\Theta_n),$$

$$|\sin \Theta(k_{ib,n})| \approx |\delta\Theta_n|, \quad \text{and}$$

$$\delta\Theta_n = 2\pi \frac{k_n - k_{ib,n}}{k_{n+1} - k_{n-1}}, \quad (\text{B3})$$

where we use the fact that there is a change in the phase of  $\Theta$  by  $2\pi$  from the  $n - 1$  to the  $n + 1$  zero crossings. Then with common factors removed, Eq. (B2) reduces to

$$\frac{d(\sigma^2)}{dT} 2\pi \left( \frac{k_n - k_{ib,n}}{k_{n+1} - k_{n-1}} \right) = \frac{2k_{ib,n}}{3} \frac{dC_3}{dT}. \quad (\text{B4})$$

Equation (B4) shows explicitly that in the experimental data, there is a relationship between  $C_3$  and  $\sigma^2$ . Although the isosbestic points  $k_{ib,n}$  are  $T$ -independent,  $\sigma^2$  and the zero crossing  $k_n$  are functions of  $T$ , and the left hand side of Eq. (B4) can be integrated numerically to obtain  $C_3$ . Examples for the Pb  $L_{III}$  and Br  $K$  edges are shown in Fig. 11. All plots were normalized at 70 K. Because we only have a small number of temperature points, this integration is a crude estimate of  $C_3$ , but clearly shows that  $C_3$  is related to  $\sigma^2$ . Note also that the value of  $C_3$  is very sensitive to the value of  $k_{ib,n}$ , as the left side of Eq. (B4) is proportional to  $k_n - k_{ib,n}$ ; this difference is small and small variations in  $k_{ib,n}$  have a large affect on  $k_n - k_{ib,n}$ . To show this sensitivity clearly, the integral has been evaluated with  $k_{ib,n}$  varied by  $\pm 0.2\%$  for Pb and  $\pm 0.3\%$  for Br—see dotted red lines in Fig. 11. For the Pb  $L_{III}$  edge we have also included in Fig. 11(a), the values of  $C_3$  (blue triangles) obtained using the zero crossings analysis outlined in Appendix A. This plot shows that within the scatter the three methods are in good agreement.

- [1] H. Min, D. Y. Lee, J. Kim, G. Kim, K. S. Lee, J. Kim, M. J. Paik, Y. K. Kim, K. S. Kim, M. G. Kim, T. J. Shin, and S. I. Seok, *Nature (London)* **598**, 444 (2021).
- [2] R. Lin, J. Xu, M. Wei, Y. Wang, Z. Qin, Z. Liu, J. Wu, K. Xiao, B. Chen, S. M. Park, G. Chen, H. R. Atapattu, K. R. Graham, J. Xu, J. Zhu, L. Li, C. Zhang, E. H. Sargent, and H. Tan, *Nature (London)* **603**, 73 (2022).
- [3] S. Hirotsu, J. Harada, M. Iizumi, and K. Gesi, *J. Phys. Soc. Jpn.* **37**, 1393 (1974).
- [4] P. S. Whitfield, N. Herron, W. E. Guise, K. Page, Y. Q. Cheng, I. Milas, and M. K. Crawford, *Sci. Rep.* **6**, 35685 (2016).
- [5] M. T. Weller, O. J. Weber, P. F. Henry, A. M. D. Pumpo, and T. C. Hansen, *Chemical Communications* **51**, 4180 (2015).
- [6] M. Songvilay, Z. Wang, V. G. Sakai, T. Guidi, M. Bari, Z.-G. Ye, G. Xu, K. L. Brown, P. M. Gehring, and C. Stock, *Phys. Rev. Mater.* **3**, 125406 (2019).
- [7] Y. Guo, O. Yaffe, T. D. Hull, J. S. Owen, D. R. Reichman, and L. E. Brus, *Nat. Commun.* **10**, 1175 (2019).
- [8] I. P. Swainson, R. P. Hammond, C. Soullière, O. Knop, and W. Massa, *J. Solid State Chem.* **176**, 97 (2003).
- [9] I. P. Swainson, C. Stock, S. F. Parker, L. VanEijck, M. Russina, and J. W. Taylor, *Phys. Rev. B* **92**, 100303(R) (2015).
- [10] E. M. Mozur, J. C. Trowbridge, A. E. Maughan, M. J. Gorman, C. M. Brown, T. R. Prisk, and J. R. Neilson, *ACS Materials Lett.* **1**, 260 (2019).

- [11] A. Franz, D. M. Töbrens, F. Lehmann, M. Kärger, and S. Schorr, *Acta Crystallogr., Sect. B: Struct. Sci* **76**, 267 (2020).
- [12] T. Chen, B. J. Foley, B. Ipek, M. Tyagi, J. R. D. Copley, C. M. Brown, J. J. Choi, and S.-H. Lee, *Phys. Chem. Chem. Phys.* **17**, 31278 (2015).
- [13] H. Singh, R. Fei, Y. Rakita, M. Kulbak, D. Cahen, A. M. Rappe, and A. I. Frenkel, *Phys. Rev. B* **101**, 054302 (2020).
- [14] G. Schuck, D. M. Töbrens, D. Wallacher, N. Grimm, T. S. Tien, and S. Schorr, *J. Phys. Chem. C* **126**, 5388 (2022).
- [15] G. Laurita, D. H. Fabini, C. C. Stoumpos, M. G. Kanatzidis, and R. Seshadri, *Chem. Sci.* **8**, 5628 (2017).
- [16] N. J. Weadock, C. MacKeen, X. Qin, L. Waquier, Y. Rakita, J. A. Vigil, H. I. Karunadasa, V. Blum, M. F. Toney, and F. Bridges, *PRX Energy* **2**, 033004 (2023).
- [17] C. H. Booth, F. Bridges, E. D. Bauer, G. G. Li, J. B. Boyce, T. Claeson, C. W. Chu, and Q. Xiong, *Phys. Rev. B* **52**, R15745 (1995).
- [18] P. A. Lee and G. Beni, *Phys. Rev. B* **15**, 2862 (1977).
- [19] B. K. Teo, *EXAFS: Basic Principles and Data Analysis* (Springer-Verlag, New York, 1986).
- [20] *X-Ray Absorption: Principles, Applications, Techniques of EXAFS, SEXAFS, XANES*, edited by D. Koningsberger and R. Prins (Wiley, New York, 1988).
- [21] S. Zeiske, O. J. Sandberg, N. Zarrabi, C. M. Wolff, M. Raoufi, F. Peña-Camargo, E. Gutierrez-Partida, P. Meredith, M. Stolterfoht, and A. Armin, *J. Phys. Chem. Lett.* **13**, 7280 (2022).
- [22] G. Reuveni, Y. Diskin-Posner, C. Gehrman, S. Godse, G. G. Gkikas, I. Buchine, S. Aharon, R. Korobko, C. C. i Stoumpos, D. A. Egger, and O. Yaffe, *J. Phys. Chem. Lett.* **14**, 1288 (2023).
- [23] J. Liu, A. E. Phillips, D. A. Keen, and M. T. Dove, *J. Phys. Chem. C* **123**, 14934 (2019).
- [24] E. A. Stern, P. Livins, and Z. Zhang, *Phys. Rev. B* **43**, 8850 (1991).
- [25] D. Ceratti, Y. Rakitas, L. Cremonesi, R. Tenne, V. Kalchenko, M. Elbaum, D. Oron, C. P. M. A, G. Hodes, and D. Cahen, *Adv. Mater.* **30**, 1706273 (2018).
- [26] Y. Rakita, N. Kedem, S. Gupta, A. Sadhanala, V. Kalchenko, M. L. Böhm, M. Kulbak, R. H. Friend, D. Cahen, and G. Hodes, *Cryst. Growth Des.* **16**, 5717 (2016).
- [27] C. H. Booth, R-Space x-ray Absorption Package, 2010, <https://sites.google.com/lbl.gov/rsxap>.
- [28] See Supplemental Material at <http://link.aps.org/supplemental/10.1103/PhysRevB.108.214102> for *k*-space data and additional details about the data reduction and analysis.
- [29] R. T. Downs, *Rev. Mineral. Geochem.* **41**, 61 (2000).
- [30] C. H. Booth, F. Bridges, J. B. Boyce, T. Claeson, B. M. Lairson, R. Liang, and D. A. Bonn, *Phys. Rev. B* **54**, 9542 (1996).
- [31] P. Fornasini and R. Grisenti, *J. Synchrotron Radiat.* **22**, 1242 (2015).
- [32] G. M. Sheldrick, *Acta Crystallogr A Found Adv.* **71**, 3 (2015).
- [33] C. A. López, C. Abia, M. C. Alvarez-Galván, B.-K. Hong, M. V. Martínez-Huerta, F. Serrano-Sánchez, F. Carrascoso, A. Castellanos-Gómez, M. T. Fernández-Díaz, and J. A. Alonso, *ACS Omega* **5**, 5931 (2020).
- [34] S. Liu, A. R. DeFilippo, M. Balasubramanian, Z. Liu, S. G. Wang, Y.-S. Chen, S. Chariton, V. Prakapenka, X. Luo, L. Zhao, J. S. Martin, Y. Lin, Y. Yan, S. K. Ghose, and T. A. Tyson, *Adv. Sci.* **8**, 2003046 (2021).
- [35] A. Sharenko, C. Mackeen, L. Jewell, F. Bridges, and M. F. Toney, *Chem. Mater.* **29**, 1315 (2017).
- [36] G. Bunker, *Nucl. Instrum. Methods* **207**, 437 (1983).
- [37] J. M. Tranquada and R. Ingalls, *Phys. Rev. B* **28**, 3520 (1983).
- [38] D. S. Yang, D. R. Fazzini, T. I. Morrison, L. Tröger, and G. Bunker, *J. Non-Cryst. Solids* **210**, 275 (1997).
- [39] T. M. Hayes and J. B. Boyce, in *Solid State Physics* (Academic, New York, 1982), Vol. 37, p. 173.
- [40] A. L. Ankudinov and J. J. Rehr, *Phys. Rev. B* **56**, R1712 (1997).
- [41] A. Bianconi, in *x-ray Absorption: Principles, Applications, Techniques of EXAFS, SEXAFS and XANES*, edited by D. C. Koningsberger and R. Prins (John Wiley and Sons, New York, 1988), p. 594.
- [42] I. D. Brown and K. K. Wu, *Acta Crystallogr B Struct. Sci.* **32**, 1957 (1976).
- [43] I. D. Brown, in *Structure and Bonding in Crystals, Vol. II*, edited by M. O’Keeffe and A. Navrotsky (Academic Press, New York, 1981).
- [44] I. D. Brown and D. Altermatt, *Acta Crystallogr B Struct. Sci.* **41**, 244 (1985).
- [45] A. M. A. Leguy, J. M. Frost, A. P. McMahon, V. G. Sakai, W. Kockelmann, C.-H. Law, X. Li, F. Foglia, A. Walsh, B. C. O’Regan, J. Nelson, J. T. Cabral, and P. R. F. Barnes, *Nat. Commun.* **6**, 7124 (2015).
- [46] B. Yang, W. Ming, M.-H. Du, J. K. Keum, A. A. Poretzky, C. M. Rouleau, J. Huang, D. B. Geohegan, X. Wang, and K. Xiao, *Adv. Mater.* **30**, 1705801 (2018).
- [47] G. Schuck, F. Lehmann, J. Ollivier, H. Mutka, and S. Schorr, *J. Phys. Chem. C* **123**, 11436 (2019).
- [48] P. Fornasini, R. Grisenti, M. Dapiaggi, G. Agostini, and T. Miyanaga, *J. Chem. Phys.* **147**, 044503 (2017).
- [49] P. Fornasini, F. Monti, and A. Sanson, *J. Synchrotron Rad.* **8**, 1214 (2001).
- [50] T. Yokoyama and S. Chaveanghong, *Phys. Rev. Mater.* **3**, 033607 (2019).
- [51] D. Ghosh, P. W. Atkins, M. S. Islam, A. B. Walker, and C. Eames, *ACS Energy Lett.* **2**, 2424 (2017).
- [52] S. Govinda, B. Kore, D. Swain, A. Hossain, C. De, T. Row, and D. Sarma, *J. Phys. Chem. C* **122**, 13758 (2018).
- [53] B. K. Teo, H. S. Chen, R. Wang, and M. R. Antonio, *J. Non-Cryst. Solids* **58**, 249 (1983).
- [54] L. Downward, C. H. Booth, W. W. Lukens, and F. Bridges, *AIP Conf. Proc.* **882**, 129 (2007).